Beam test evaluation of electromagnetic calorimeter modules made from proton-damaged $PbWO_4$ crystals

2016 JINST 11 P04012

(http://iopscience.iop.org/1748-0221/11/04/P04012)

Jinst

Published by IOP Publishing for Sissa Medialab

Received: *January 25, 2016*
Revised: *February 26, 2016*
Accepted: *March 21, 2016*
Published: *April 11, 2016*

Beam test evaluation of electromagnetic calorimeter modules made from proton-damaged $PbWO_4$ crystals

T. Adams,[p] **P. Adzic,**[ax] **S. Ahuja,**[an] **D. Anderson,**[f] **M.B. Andrews,**[g] **I. Antropov,**[ag] **Z. Antunovic,**[aq] **R. Arcidiacono,**[au,ba] **M.W. Arenton,**[ay] **S. Argirò,**[au,ba] **A. Askew,**[p] **A. Attikis,**[ac] **E. Auffray,**[h] **S. Baccaro,**[al] **S. Baffioni,**[ag] **D. Bailleux,**[o] **P. Baillon,**[h] **D. Barney,**[h] **L. Barone,**[al] **A. Bartoloni,**[al] **N. Bartosik,**[au,ba] **E. Becheva,**[ag] **S. Bein,**[p] **C. Beirão Da Cruz E Silva,**[t] **K.W. Bell,**[ak] **A. Benaglia,**[ah] **J. Bendavid,**[f] **D. Berry,**[ae] **M. Besancon,**[am] **B. Betev,**[ao] **W. Bialas,**[h] **L. Bianchini,**[az] **C. Biino,**[au,ba] **S. Bitioukov,**[ai] **A. Bornheim,**[f] **L. Brianza,**[w] **A. Brinkerhoff,**[ae] **R.M. Brown,**[ak] **A. Brummitt,**[ak] **P. Busson,**[ag] **V. Candelise,**[av] **C.A. Carrillo Montoya,**[v] **N. Cartiglia,**[au,ba] **F. Cavallari,**[al] **Y.W. Chang,**[ar] **K.F. Chen,**[ar] **G. Chevenier,**[o] **R. Chipaux,**[am] **E. Clement,**[c] **D.J.A. Cockerill,**[ak] **L. Corpe,**[u] **F. Couderc,**[am] **B. Courbon,**[v] **B. Cox,**[ay] **G. Cucciati,**[h] **D. Cussans,**[c] **G. D'imperio,**[al] **D.R. Da Silva Di Calafiori,**[az] **I. Dafinei,**[al] **J. Daguin,**[h] **G. Daskalakis,**[m] **A.D. Tinoco Mendes,**[h] **F. De Guio,**[h] **A. Degano,**[au,ba] **M. Dejardin,**[am] **D. Del Re,**[al] **G. Della Ricca,**[av] **D. Denegri,**[am] **P. Depasse,**[v] **N. Dev,**[ae] **D. Deyrail,**[h] **E. Di Marco,**[h] **B. Diamond,**[p] **M. Diemoz,**[al] **G. Dissertori,**[az] **M. Dittmar,**[az] **L. Djambazov,**[az] **T.H. Doan,**[j] **L. Dobrzynski,**[ag] **A. Dolgopolov,**[o] **M. Donegà,**[az] **M. Dordevic,**[h] **M. Dröge,**[az] **T. Durkin,**[ak] **D. Dutta,**[s] **H. El Mamouni,**[v] **A. Elliott-Peisert,**[h] **E. Elmalis,**[m] **B. Fabbro,**[am] **G. Fasanella,**[e] **J. Faure,**[am] **J. Fay,**[v] **A. Fedorov,**[y] **F. Ferri,**[am] **B. Francis,**[ay] **N. Frank,**[h] **G. Franzoni,**[h] **W. Funk,**[h] **S. Ganjour,**[am] **S. Gascon,**[v] **M. Gastal,**[h] **Y. Geerebaert,**[ag] **S. Gelli,**[al] **R. Gerosa,**[aw] **A. Ghezzi,**[w] **V.A. Giakoumopoulou,**[m] **A. Givernaud,**[am] **S. Gninenko,**[aa] **N. Godinovic,**[ap] **N. Goeckner-Wald,**[g] **N. Golubev,**[aa] **P. Govoni,**[w] **P. Gras,**[am] **F. Guilloux,**[am] **C. Haller,**[az] **G. Hamel de Monchenault,**[am] **M. Hansen,**[h] **P. Hansen,**[x] **J. Hardenbrook,**[ah] **H.F. Heath,**[c] **J. Hill,**[ak] **R. Hirosky,**[ay] **P.R. Hobson,**[d] **O. Holme,**[az] **A. Honma,**[h] **W.-S. Hou,**[ar] **Y. Hsiung,**[ar] **Y. Iiyama,**[z] **B. Ille,**[v] **Q. Ingram,**[aj] **S. Jain,**[at] **P. Jarry,**[am] **C. Jessop,**[ae] **D. Jovanovic,**[ax] **V. Kachanov,**[ai] **S. Kalafut,**[x] **K.Y. Kao,**[ar] **N. Kellams,**[ae] **S. Kesisoglou,**[a] **A. Khatiwada,**[p] **A. Konoplyannikov,**[h] **D. Konstantinov,**[ai] **M. Korzhik,**[y] **M. Kovac,**[aq] **Y. Kubota,**[x] **I. Kucher,**[am] **A. Kumar,**[l] **A. Kumar,**[ar] **C. Kuo,**[j] **P. Kyberd,**[d] **A. Kyriakis,**[m] **G. Latyshev,**[ai] **P. Lecoq,**[h] **A. Ledovskoy,**[ay] **Y.J. Lei,**[ar] **D. Lelas,**[ap] **M. Lethuillier,**[v] **H. Li,**[ay] **W. Lin,**[j] **Y.F. Liu,**[ar] **E. Locci,**[am] **E. Longo,**[al] **D. Loukas,**[m] **R.-S. Lu,**[ar] **M.T. Lucchini,**[h,1] **W. Lustermann,**[az] **C.K. Mackay,**[d] **F. Magniette,**[ag] **J. Malcles,**[am] **S. Malhotra,**[l] **I. Mandjavidze,**[am] **Y. Maravin,**[r] **F. Margaroli,**[al] **N. Marinelli,**[ae] **A.C. Marini,**[z] **A. Martelli,**[h]

[1]Corresponding author.

doi:10.1088/1748-0221/11/04/P04012

2016 JINST 11 P04012

B. Marzocchi,[w] A. Massironi,[ad] V. Matveev,[n] V. Mechinsky,[y] F. Meng,[ae] P. Meridiani,[al] F. Micheli,[az] J. Milosevic,[ax] J. Mousa,[ac] P. Musella,[az] F. Nessi-Tedaldi,[az] C. Neu,[ay] H. Newman,[f] C. Nicolaou,[ac] S. Nourbakhsh,[x] M.M. Obertino,[au,ba] G. Organtini,[al] T. Orimoto,[ad] P. Paganini,[ag] E. Paganis,[ar] M. Paganoni,[w] F. Pandolfi,[az] V. Panov,[y] R. Paramatti,[al] P. Parracho,[h] N. Pastrone,[au,ba] M. Paulini,[g] F. Pauss,[az] K. Pauwels,[h] F. Pellegrino,[al] C. Pena,[f] L. Perniè,[as] M. Peruzzi,[h] E. Petrakou,[ar] D. Petyt,[ak] S. Pigazzini,[w] P. Piroué,[ah] M. Planer,[ae] R. Plestina,[b] D. Polic,[ap] H. Prosper,[p] F. Ptochos,[ac] I. Puljak,[ap] M. Quittnat,[az] S. Ragazzi,[w] S. Rahatlou,[al] J. Rander,[am] K. Ranjan,[l] J. Rasteiro Da Silva,[t] P.A. Razis,[ac] T. Romanteau,[ag] A. Rosowsky,[am] C. Rovelli,[al] R. Rusack,[x] R. Salerno,[ag] F. Santanastasio,[al] A. Santra,[p] M. Schönenberger,[az] C. Seez,[u] V. Sharma,[l] C. Shepherd-Themistocleous,[ak] J.G. Shiu,[ar] R.K. Shivpuri,[l] A. Singovsky,[x] T. Sinthuprasith,[ay] Y. Sirois,[ag] N. Smiljkovic,[ax] L. Soffi,[k] M. Sun,[g] P. Symonds,[d] T. Tabarelli de Fatis,[w] N. Tambe,[x] I. Tarasov,[h] S. Taroni,[ae] R. Teixeira De Lima,[ad] A. Thea,[ak] K. Theofilatos,[az] F. Thiant,[ag] M. Titov,[am] M. Torbet,[ak] P.P. Trapani,[au,ba] P. Tropea,[h] J.f. Tsai,[ar] A. Tsirou,[h] J. Turkewitz,[x] N. Tyurin,[ai] Y.M. Tzeng,[ar] A. Uzunian,[ai] N. Valls,[ae] J. Varela,[t] V. Veeraraghavan,[p] P.G. Verdini,[af] P. Vichoudis,[h] E. Vlassov,[ab] J. Wang,[p] T. Wang,[z] M. Weinberg,[p] E. Wolfe,[ay] J. Wood,[aw] A. Zabi,[ag] S. Zahid,[d] S. Zelepoukine,[az] A. Zghiche,[am] L. Zhang,[f] K. Zhu,[f] R. Zhu[f] and R. Zuyeuski[y]

[a] *University of Athens, Panepistimiopolis, Ilissia, Athens, 15771 Greece*

[b] *Institute of High Energy Physics, 19B Yuquan Lu, Shijingshan District, Beijing, 100049 China*

[c] *University of Bristol, Senate House, Tyndall Ave, Bristol, BS8 1TH United Kingdom*

[d] *Brunel University, Kingston Ln, Uxbridge, Middlesex, UB8 3PH United Kingdom*

[e] *Université libre de Bruxelles, Franklin Rooseveltlaan 50, Bruxelles, 1050 Belgium*

[f] *California Institute of Technology, 1200 E California Blvd, Pasadena, CA, 91125 U.S.A.*

[g] *Carnegie Mellon University, 5000 Forbes Ave, Pittsburgh, Pennsylvania, 15213 U.S.A.*

[h] *CERN, European Organization for Nuclear Research, Geneva 23, CH-1211 Switzerland*

[j] *National Central University, No. 300, Zhongda Rd, Chung-Li, 320 Taiwan*

[k] *Cornell University, 144 East Ave., Ithaca, New York, 14850 U.S.A.*

[l] *University of Delhi, Delhi, 110007 India*

[m] *Institute of Nuclear Physics 'Demokritos', 27 Neapoleos str., Attiki, Athens, Greece*

[n] *Joint Institute for Nuclear Research, Joliot-Curie, 6, Dubna, Russia*

2016 JINST 11 P04012

[o] *Fermi National Accelerator Laboratory,*
Wilson Street & Kirk Road, Batavia, Illinois, 60510 U.S.A.
[p] *Florida State University,*
600 W College Ave, Tallahassee, Florida, 32306 U.S.A.
[r] *Kansas State University,*
Manhattan, Kansas, 66506 U.S.A.
[s] *Saha Institute of Nuclear Physics, Block-AF, Sector-1,*
Bidhan nagar, Kolkata, West Bengal, 700064 India
[t] *Laboratório de Instrumentação e Física Experimental de Partículas,*
Av. Elias Garcia 14, Lisboa, 1000 Portugal
[u] *Imperial College, University of London,*
London, SW7 2AZ United Kingdom
[v] *Institut de Physique Nucléaire, IN2P3-CNRS and Université C. Bernard Lyon I,*
4 Rue Enrico Fermi, Villeurbanne, 69622 France
[w] *INFN Sezione di Milano-Bicocca and Università di Milano-Bicocca,*
Piazza della Scienza 3, Milano, 20126 Italy
[x] *University of Minnesota,*
3 Morrill Hall 100 Church St. S.E., Minneapolis, Minnesota, U.S.A.
[y] *Research Institute for Nuclear Problems, Byelorussian State University,*
Bobruiskaya str. 11, Minsk, 220030 Belarus
[z] *Massachusetts Institute of Technology,*
77 Massachusetts Ave, Cambridge, Massachusetts, 02139 U.S.A.
[aa] *Institute for Nuclear Research, Russian Academy of Sciences,*
60th October Anniversary pr., 7a, Moscow, 117312 Russia
[ab] *Institute for Theoretical and Experimental Physics,*
Bolshaya Cheremushkinskaya ul., Moscow, 25c2 Russia
[ac] *University of Cyprus,*
1 Panepistimiou Avenue, Aglantzia, Nicosia, 2109 Cyprus
[ad] *Northeastern University,*
360 Huntington Ave, Boston, Massachusetts, 02115 U.S.A.
[ae] *University of Notre Dame,*
Notre Dame, Indiana, 46556 U.S.A.
[af] *INFN-Sezione di Pisa,*
Largo Bruno Pontecorvo, 3, Pisa, 56127 Italy
[ag] *Laboratoire Leprince-Ringuet, Ecole Polytechnique,*
Avenue Chasles, Palaiseau, Cedex 91120 France
[ah] *Princeton University,*
Princeton, New Jersey, 08544 U.S.A.
[ai] *State Research Center of Russian Federation — Institute for High Energy Physics,*
Protvino, Moscow, 142281 Russia
[aj] *Paul Scherrer Institut (PSI),*
Villigen, 5232 Switzerland
[ak] *Rutherford Appleton Laboratory, Science and Technology Facilities Council,*
Harwell Campus, Didcot, OX11 0QX United Kingdom
[al] *INFN Sezione di Roma and Sapienza Università di Roma,*
P.le Aldo Moro, 2, Roma, 00185 Italy

2016 JINST 11 P04012

[am] *DSM/DAPNIA, CEA/Saclay,*
Gif-sur-Yvette, Cedex 91191 France
[an] *Universidade Estadual Paulista,*
R. Pamplona, 145, São Paulo, Brazil
[ao] *Institute of Systems Engineering and Robotics,*
G. Bonchev str., Sofia, Bulgaria
[ap] *University of Split, Faculty of Electrical Engineering, Mechanical Engineering and Naval Architecture,*
R. Boškovića 32, Split, 21000 Croatia
[aq] *University of Split, Faculty of Science,*
Livanjska 5, Split, 21000 Croatia
[ar] *National Taiwan University,*
4, Roosevelt Rd, Da'an District, Taipei, Taiwan
[as] *Texas A&M University,*
400 Bizzell St, College Station, Texas, 77840 U.S.A.
[at] *Bhabha Atomic Research Centre,*
Trombay, Mumbai, India
[au] *INFN Sezione di Torino, Università di Torino,*
Via Pietro Giuria, 1, Torino, 10125 Italy
[av] *INFN Sezione di Trieste and Università di Trieste,*
Padriciano, 99, Trieste, 34149 Italy
[aw] *University of California,*
Gilman Dr., San Diego, California, 9500 U.S.A.
[ax] *'Vinca' Institute of Nuclear Sciences and Faculty of Physics of University of Belgrade,*
P.O. Box 522, Belgrade, 11001 Serbia
[ay] *The University of Virginia,*
Charlottesville, Virginia, 22904-4246 U.S.A.
[az] *Institute for Particle Physics, ETH Zurich,*
Otto-Stern-Weg 5, Zurich, 8093 Switzerland
[ba] *Università del Piemonte Orientale,*
Via Duomo, 6, Novara, 13100 Italy

E-mail: marco.toliman.lucchini@cern.ch

2016 JINST 11 P04012

Abstract: The performance of electromagnetic calorimeter modules made of proton-irradiated $PbWO_4$ crystals has been studied in beam tests. The modules, similar to those used in the Endcaps of the CMS electromagnetic calorimeter (ECAL), were formed from 5×5 matrices of $PbWO_4$ crystals, which had previously been exposed to 24 GeV protons up to integrated fluences between 2.1×10^{13} and 1.3×10^{14} cm^{-2}. These correspond to the predicted charged-hadron fluences in the ECAL Endcaps at pseudorapidity $\eta = 2.6$ after about 500 fb^{-1} and 3000 fb^{-1} respectively, corresponding to the end of the LHC and High Luminosity LHC operation periods. The irradiated crystals have a lower light transmission for wavelengths corresponding to the scintillation light, and a correspondingly reduced light output. A comparison with four crystals irradiated in situ in CMS showed no significant rate dependence of hadron-induced damage. A degradation of the energy resolution and a non-linear response to electron showers are observed in damaged crystals. Direct measurements of the light output from the crystals show the amplitude decreasing and pulse becoming faster as the fluence increases. The latter is interpreted, through comparison with simulation, as a side-effect of the degradation in light transmission. The experimental results obtained can be used to estimate the long term performance of the CMS ECAL.

Keywords: Calorimeters; Scintillators, scintillation and light emission processes (solid, gas and liquid scintillators); Radiation-hard detectors; Detector modelling and simulations I (interaction of radiation with matter, interaction of photons with matter, interaction of hadrons with matter, etc)

2016 JINST 11 P04012

Contents

2016 JINST 11 P04012

1 Introduction

The CMS [1] Electromagnetic Calorimeter (ECAL [2]) is a homogeneous device based on $PbWO_4$ scintillating crystals. These crystals emit blue-green scintillation light with a broad maximum at wavelengths 420–430 nm. This light is detected by Avalanche Photodiodes (APDs) in the barrel (EB) and Vacuum Phototriodes (VPTs) in the endcaps (EE). The EB covers the pseudorapidity range $|\eta| < 1.5$ with the EE extending the coverage to $|\eta| < 3.0$.

The ECAL was designed to operate at the CERN LHC with an instaneous luminosity of $\mathcal{L} = 1 \times 10^{34}$ cm^{-2}s^{-1} and to collect 500 fb^{-1} of proton-proton collisions at $\sqrt{s} = 14$ TeV. A particular challenge was to maintain excellent performance despite unprecedented levels of radiation: electromagnetic dose rates up to 0.2 Gy/h in EB (at $|\eta| = 1.5$) and 6 Gy/h in EE (at $|\eta| = 2.6$); and charged hadron fluences of up to 1.2×10^{11} cm^{-2} in EB and 3×10^{13} cm^{-2} in EE [1, 2]. The original scope of the LHC project has, during the past few years, increased substantially and now includes a High Luminosity phase ("HL-LHC") that will take the integrated luminosity to around 3000 fb^{-1} and the instantaneous luminosity to about $\mathcal{L} = 5 \times 10^{34}$ cm^{-2}s^{-1}. The HL-LHC is due to start around 2025 and last until at least 2035 when the integrated luminosity of around 3000 fb^{-1} will be achieved.

The corresponding dose rates and hadron fluences are predicted to be a factor of ~6 higher than the ECAL was designed for, by the end of HL-LHC operation [1, 3]. Thus the crystals can expect to experience a hadron fluence of the order of $\sim 7 \times 10^{11}$ cm^{-2} at $\eta = 1.5$ and $\sim 2 \times 10^{14}$ cm^{-2} at $\eta = 2.6$. The radiation hardness of the crystals is one of the most crucial aspects to consider in understanding the performance evolution of the calorimeter.

$PbWO_4$ crystals suffer from both electromagnetic-induced (em-induced) and hadron-induced damage. Both types of damage lead to losses of crystal transparency at relevant wavelengths, but the fundamental scintillation mechanism is not degraded [4–6]. The LHC has currently (circa 2015) delivered around 30 fb^{-1} of proton-proton collisions, around 1% of the total expected by the end of HL-LHC. The em-induced damage presently dominates, with indications of hadron-induced damage only at the highest pseudorapidity. During the coming years the hadron-induced damage will become significant for most of the pseudorapidity coverage of the ECAL. For HL-LHC, the hadron-induced damage is expected to dominate the transparency loss crystals at large pseudorapidity ($|\eta| > 2$).

The ECAL crystals were optimized for their application in CMS, particularly with respect to radiation hardness through many studies with ionizing electromagnetic radiation and hadrons [7]. This optimization was done through stoichiometry, doping the $PbWO_4$ with small amounts of yttrium and niobium [8].

The effects of ionizing electromagnetic radiation on lead tungstate were studied in depth using γ radiation from ^{60}Co sources. The crystal light transmission is reduced through the formation of colour centres. The crystal transparency largely recovers through spontaneous annealing at the ECAL operating temperature of 18°C [7]. The residual damage, defined as the light output reduction due to a loss in the light transmission, depends on the balance between damage and recovery rates [7].

Hadron-induced damage is significantly different from em-induced damage [9–14]. Firstly, there is practically no recovery at the ECAL operating temperature; hence the damage is cumulative. Secondly, the transmission band edge is shifted by several tens of nanometers to higher values and starts to overlap with the scintillation emission peak. These effects make the hadron-induced damage more crucial since it can lead to significant losses of the crystal light transmission.

A high precision light monitoring system, using injected laser light at 447 nm, is used to track and correct for response changes during LHC operation, minimizing the contribution to the ECAL energy resolution from radiation damage. At present the contribution to the energy resolution is below 0.3% [15].

2016 JINST 11 P04012

In addition to the light output loss due to radiation damage, the uniformity of the light collection efficiency along the length of the crystal decreases. For a non-irradiated crystal, the tapered geometry partially compensates for the effect of light absorption and helps maintain the light collection non-uniformity below $0.35\%/X_0$ [2]. The light originating from near the photodetector will have higher probability of collection, as light produced further away is more likely to be absorbed by the crystal. This effect will produce a degradation of the constant term of the energy resolution, which cannot be corrected for.

This paper summarizes several laboratory, in-situ (in CMS) and beam-test measurements, to evaluate the performance of $PbWO_4$ crystals in the regime in which hadron-induced damage dominates. The irradiations and subsequent crystal characterization measurements are described in section 2, as well as the correlation between proton fluence and light-induced absorption. The experimental setups, including the arrays of irradiated crystals used for the beam tests, is described in section 3. The data analysis procedure is presented in section 4 and leads to a detailed picture of the effects induced by hadron damage in $PbWO_4$ crystals, which is discussed in section 5. The set of results presented provide important information to evaluate the CMS ECAL performance degradation with time and accumulated fluence.

2 Irradiation and characterization of crystals

In order to explore the effects of hadron-induced damage to $PbWO_4$ crystals, several irradiation campaigns have taken place over the past few years, using spare crystals from the CMS production. A total of 24 crystals were irradiated.

Most of the irradiations took place at the CERN Proton Synchrotron facility, which provides a high intensity monochromatic source of high-energy (24 GeV) protons. The full expected fluence at high η at the end of HL-LHC can be provided in a few days with this beam. Four crystals were also irradiated in the CMS experimental cavern in 2012, being placed close to the beam pipe on a table that normally supports the CASTOR [16] detector. The particle types and energy spectra that caused damage to these crystals is similar to that inside CMS. The two crystals closest to the beam pipe received, in approximately eight months, about a third of the fluence expected at high η at the end of HL-LHC. With these two sets of irradiations it is possible to determine whether there is a significant rate-dependence to the radiation damage. In addition, a comparison between these two types of irradiation allows to prove that 24 GeV proton irradiation can be representative of the real damage occuring in the CMS detector.

Prior to the irradiations, each crystal underwent a detailed characterization using the ACCOS [17] spectrophotometer, originally used for the quality control of the production CMS ECAL crystals. This characterization was repeated after the irradiations.

2.1 Proton irradiation at the CERN Proton Synchrotron

Sets of $PbWO_4$ crystals with the same dimensions as those used in the EE (rear face: 30×30 mm^2; 220 mm long truncated pyramids) were irradiated with 24 GeV protons at the Proton Synchrotron (PS) IRRAD3 facility at CERN [18] in 2011 and 2012. The average proton flux through the crystal front face was 10^9 s^{-1}cm^{-2}. The full expected fluence at $\eta = 2.6$ at the end of HL-LHC can thus be

2016 JINST 11 P04012

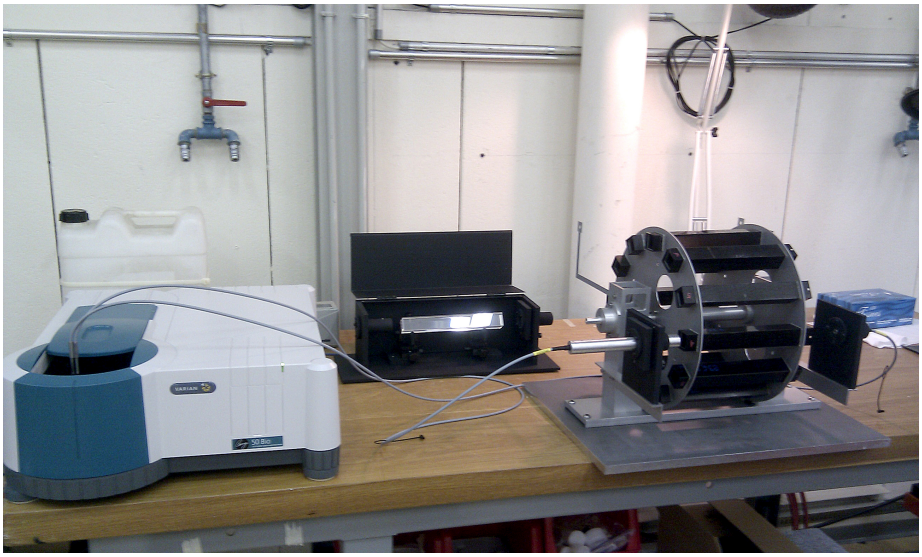

Figure 1. The revolving barrel that allowed 12 black-wrapped crystals to be irradiated in series in the IRRAD3 facility at CERN. The same structure was used to perform light transmission measurements using the spectrophotometer (shown on the left).

reached in about 56 hours. A remotely-controlled "revolving barrel", as shown in figure 1, allowed up to 12 crystals to be irradiated one after the other, without having to enter the irradiation zone.

The beam profile was monitored using the standard instrumentation of the irradiation facility and was tuned before each irradiation to be approximately uniform on a $\sim 35 \times 35$ mm^2 area, to cover the full front face of the crystal being irradiated. However, a significant residual transverse non-uniformity remained during some irradiation periods, as described below. Thin aluminium foils covering the front and rear faces of the crystals enabled the proton fluence to be estimated with a precision of about 10% through a measurement of their activation [19]. Crystals have been irradiated to proton fluences ranging from 2.1×10^{13} to 1.3×10^{14} cm^{-2}. The highest fluence is limited by practical considerations: since $PbWO_4$ crystals become radioactive after proton irradiation, a "cool down" period after irradiation is necessary, to allow for a safe handling of the crystals. This period is about 3 months for the highest fluence, during which crystals were kept in the dark at room temperature to avoid recovery of hadron damage.

2.2 Light transmission measurements

The ACCOS spectrophotometer at CERN was used to measure the transmission of light through the crystals, before and after irradiation, for wavelengths in the 300–700 nm range. Since $PbWO_4$ crystals become radioactive after proton-irradiation, the light transmission measurement was performed after a period of about 3 months from irradiation, due to the aforementioned handling constraints. Room-temperature thermal annealing of hadron-induced damage over this time period is negligible. The before/after difference provides a measure of the wavelength-dependent transmission loss. A convenient single-value measure of the transmission loss is the induced absorption coefficient μ_{ind} at 420 nm, the peak of the $PbWO_4$ emission spectrum. It is defined as:

$$\mu_{\text{ind}} = \frac{1}{L} \ln \frac{T_{\text{b}}}{T_{\text{a}}} \tag{2.1}$$

2016 JINST 11 P04012

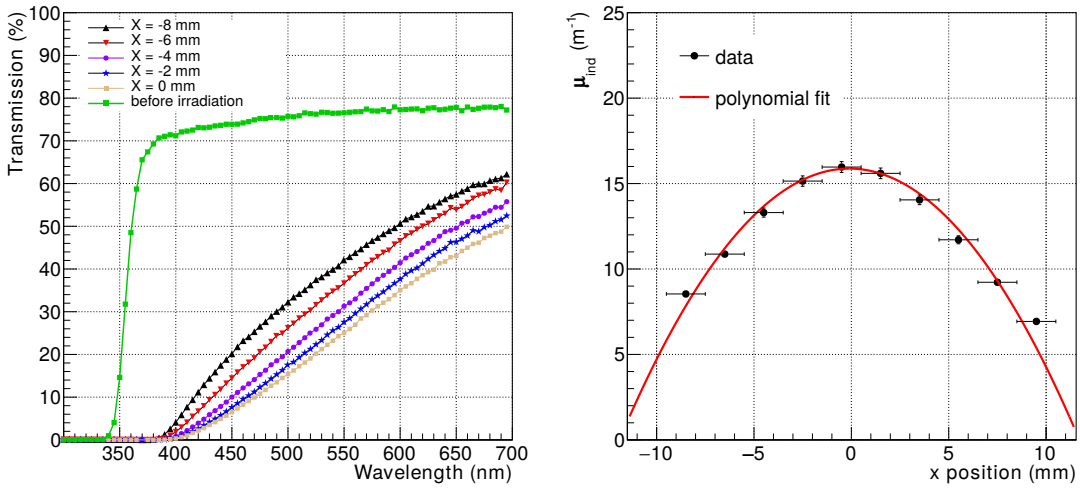

Figure 2. Left: longitudinal transmission as a function of wavelength for a crystal, irradiated to a fluence of 5.36×10^{13} p/cm^2 in 2012, at different positions on the x axis of the crystal front face. The green curve shows the transmission for a reference non-irradiated crystal. Right: corresponding transverse (x) profile of the μ_{ind} calculated from transmission curves at 420 nm for the central y position. The spectrophotometer beam spot was 2 mm in diameter. Data points are fitted using a 2$^{\text{nd}}$ order polynomial function.

where L is the crystal length (equal to 0.22 m), T_{b} and T_{a} are the crystal longitudinal light transmissions at 420 nm measured respectively before and after irradiation.

Transverse non-uniformities of the proton beam can lead to non-uniform damage of the crystals. The light transmission has been measured along the length of the crystals, as functions of the horizontal (x) and vertical (y) position on the crystal face using a dedicated spectrophotometer (different from the one described in [17]) with a collimated optical beam of 2 mm diameter. The transmission profiles were measured for all crystals for wavelengths in the 300–700 nm range and the corresponding μ_{ind} values were calculated as functions of transverse position on the front face. Comparing the light transmission at 420 nm, for different x and y positions across the crystal face, we observed a strong non-uniformity. This is demonstrated for crystal 11135, irradiated in 2012, in figure 2 and can be attributed to a residual non-uniformity of the proton beam profile used for irradiation. To take into account the transverse non-uniformity of the damage, the value of μ_{ind} used in this paper is defined as the average μ_{ind} over the whole crystal face. For 2012 crystals, the average μ_{ind} is a factor 0.48 ± 0.05 lower than the μ_{ind} measured by ACCOS in the centre of the crystal. For the crystals irradiated in 2011, the profiles are significantly more uniform and the ratio between the average and the central value is 1.04 ± 0.05. The measured values of μ_{ind} are given in section 3.2.

We estimate a 10% relative error on the estimation of μ_{ind} due to a $\sim$ 2% systematic error in the transmission measurement, which propagates via eq. (2.1). An additional uncertainty of 20% is added in quadrature to the 2012 measurements. This takes into account possible errors on the beam spot position that can lead to rather significant uncertainties on the measured μ_{ind}.

The longitudinal damage profile from 24 GeV protons was also determined, by measuring the light transmission across the width of the crystal at positions along the z axis. Examples for two

2016 JINST 11 P04012

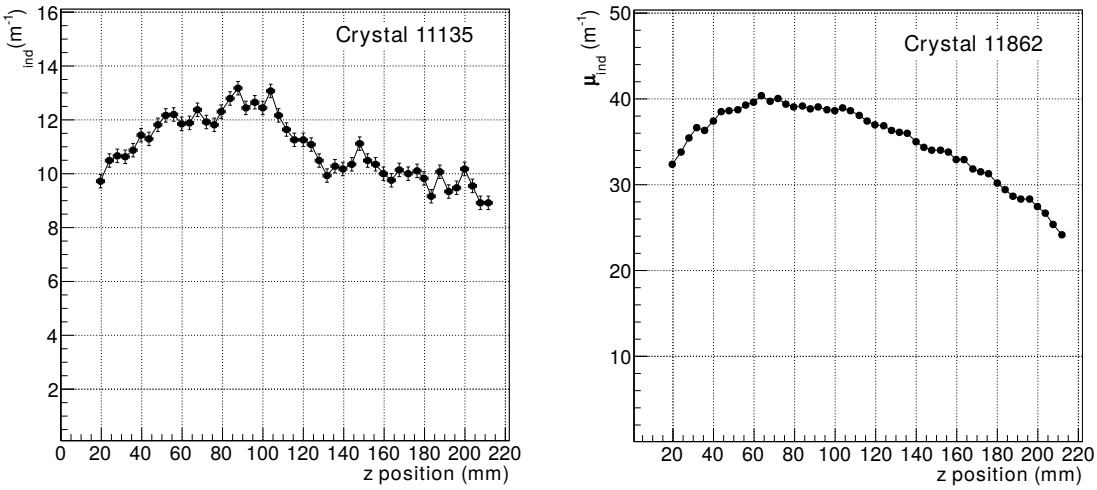

Figure 3. Longitudinal profile of the μ_{ind} for crystals irradiated to a fluence of 5.36×10^{13} p/cm^2 (left) and 1.34×10^{14} p/cm^2 (right) calculated from transmission curves at 420 nm. The spectrophotometer beam spot was 2 mm in diameter. The front face of the crystal corresponds to $z = 0$.

crystals are shown in figure 3. As expected from previous simulation studies [20], the damage is uniform to ±20% and shows a broad maximum at a distance of about 7 cm from the crystal front face, corresponding approximately to the electromagnetic shower maximum for electrons of 50–200 GeV energy.

2.3 Irradiation in the CMS detector

It is of crucial importance to demonstrate that irradiation with 24 GeV protons in a very short time at the IRRAD3 facility is representative of the damage induced by the mixture of charged hadrons occurring over many years in CMS during collisions. In particular, the longitudinal profile of damage observed in proton-irradiated crystals (figure 3) could be a specific feature of 24 GeV protons, not present in situ in CMS. This difference can play a role in the crystal performance degradation since the maximum of the damage occurs close to the shower maximum of electromagnetic particles in the 10–250 GeV range (∼ 6–7 cm).

For this reason a 2×2 matrix of endcap-sized $PbWO_4$ crystals was positioned inside the CMS experimental cavern at the end of February 2012, very close to the beam pipe, just over 14 m from the centre of CMS. The first pair of crystals (ids: 11950, 11964) was placed with their closest edges ∼7.5 cm from the centre of the beam pipe, and the second pair (11928, 11929) adjacent to these, corresponding respectively to pseudorapidities of $\eta_1 = 5.27$ and $\eta_2 = 4.93$. A schematic and photograph of the setup are shown in figure 4. The crystals were removed from CMS in the middle of January 2013. During the ∼8 months the crystals were in CMS, the LHC delivered around 25 fb^{-1} of proton-proton collisions to CMS.

A Fluka [21, 22] simulation was used to estimate the charged and neutral hadron fluences seen by these crystals. A threshold of 20 MeV was applied to select hadrons which can produce fission fragments in $PbWO_4$, and thus responsible for damage of the crystal structure [12]. The results are

2016 JINST 11 P04012

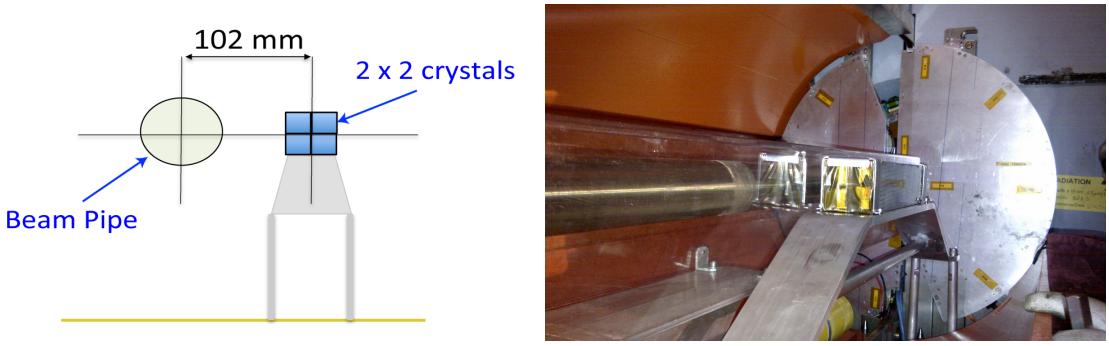

Figure 4. Schematic and photo of the 2×2 EE-sized crystals irradiated close to the CMS beam pipe in 2012.

Table 1. Estimated fluences for different types of particle as predicted from the FLUKA simulation for the two pairs of crystals at different distances from the beam pipe. The simulation energy threshold for produced hadrons is set to $E > 20$ MeV. Also shown is the measured average μ_{ind} for these crystals after irradiation.

Crystal ID	R [cm]	Protons	Neutrons	Pions	Total	μ_{ind} [m^{-1}]
11950	7.5	0.2×10^{13}	4×10^{13}	1.5×10^{13}	5.7×10^{13}	8.4
11964	7.5	0.2×10^{13}	4×10^{13}	1.5×10^{13}	5.7×10^{13}	7.6
11928	10.2	0.1×10^{13}	3.5×10^{13}	0.7×10^{13}	4.3×10^{13}	3.9
11929	10.2	0.1×10^{13}	3.5×10^{13}	0.7×10^{13}	4.3×10^{13}	3.8

shown in table 1. The total fluence (due to both charged and neutral hadrons) seen by the crystals closest to the beam pipe was estimated to be about one third of that expected at $\eta = 2.6$ at the end of HL-LHC. The error on these fluence estimations is around 30%, dominated by uncertainties in the upstream materials.

The damage profiles along the crystal z axis were measured after the crystals had been removed from CMS. Small and smooth variations of μ_{ind} as functions of the x and y light incident positions were observed (see figure 5). This non-uniformity can be attributed to the hadron fluence gradient along η, which, although stronger for crystals 11950 and 11964 (being closer to the beam pipe), is relatively small. Longitudinal profiles of damage (along crystal axis z) are also shown on the right plot of figure 5 and show a behaviour that is similar to those observed after 24 GeV proton irradiation, with a maximum of damage around 7 cm from the crystal front face.

2.4 Induced absorption vs charged hadron fluence

Figure 6 shows the induced absorbtion coefficient μ_{ind} plotted as a function of the total hadron fluence, for crystals irradiated with 24 GeV protons at the CERN PS and the crystals irradiated close to the beam pipe in the CMS experimental cavern. A correlation is observed that is consistent for all crystals and both irradiation types. A linear fit to the measurements of PS-irradiated crystals yields the following parameterization:

$$\mu_{\text{ind}} = k \times \Phi_{\text{hadrons}} \tag{2.2}$$

2016 JINST 11 P04012

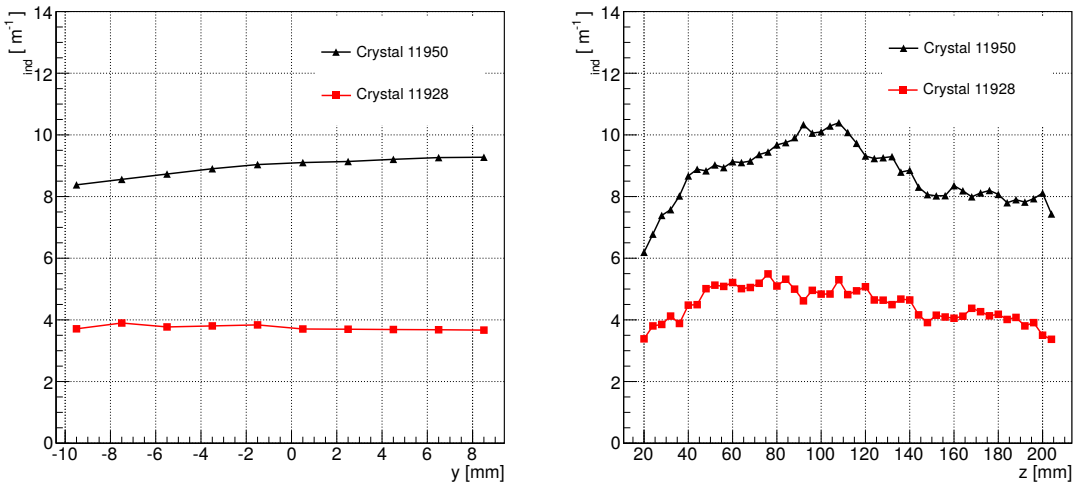

Figure 5. Damage profile across y (left) and along z (right) for crystals 11928 (red, bottom) and 11950 (black, top) irradiated in CMS at different η positions.

where Φ_{hadrons} is the total hadron fluence in cm^{-2} and the correlation coefficient is $k = (1.51 \pm 0.08) \times 10^{-13}$ cm^2/m.

We conclude from these observations that the irradiations with 24 GeV protons are a good representation of what happens in CMS, in terms of the longitudinal damage profile, and that there is little or no rate dependence on the damage. This supports the procedure of estimating the long-term performance of the CMS ECAL through beam tests of 24 GeV-protons-irradiated crystals.

3 Beam tests of irradiated crystals

These tests were used to evaluate the performance, in terms of energy resolution and energy linearity, of irradiated crystals and thus predict the expected long-term performance of the CMS ECAL.

3.1 Calorimetric module

For each beam test, twenty-five EE-sized crystals were placed inside a standard 5×5 carbon-fibre alveolar structure identical to those used in the CMS endcaps [2]. The plastic inserts in front of the crystals were the same as those used in EE, while the aluminium inserts at the photo detector side were modified to house Hamamatsu Photonics photomultipliers (PMTs) R5380 [23]. These PMTs were used for collecting and amplifying the scintillation light produced in the crystals. They were preferred over VPTs due to their higher gain and signal-to-noise, allowing accurate measurements of the small signals from highly-irradiated crystals. The PMTs have bialkali photocathodes and borosilicate glass windows of the same dimensions as the EE VPTs [2]. This means that the $PbWO_4$ scintillating light collection of the test module is close to the light collection in the EE. The radiation damage effects on the crystal light collection uniformity are therefore well reproduced and differences with respect to the EE configuration are negligible with respect to other systematic effects in the present analysis.

2016 JINST 11 P04012

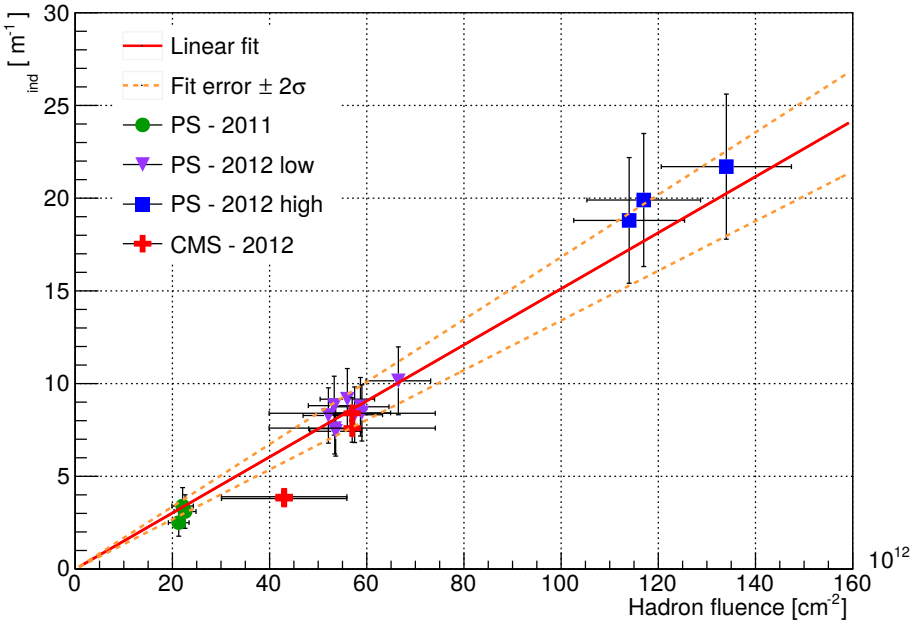

Figure 6. Correlation between the accumulated hadron fluence and the μ_{ind} for crystals irradiated at the CERN PS in 2011 and two sets of crystals irradiated in 2012 to low ($< 10^{14}\text{cm}^{-2}$) and high ($> 10^{14}\text{cm}^{-2}$) fluences. The error bars take into account both systematic uncertainties in the light transmission and fluence measurements as well as the spread in the μ_{ind} value across the crystal face. Measurements from the crystals irradiated in situ in CMS are also shown. The fit, which only uses the PS-irradiated crystals, is constrained to pass through the origin as μ_{ind} is zero for zero irradiation, by definition.

Some support structures were added to allow individual mounting of PMTs, providing a small pressure of the PMT against the crystal. The crystals were coupled to the PMT with an optical grease with refractive index 1.45, similar to the glue used to couple the EE crystals to VPTs in CMS. The alveolar structure was surrounded by 1 cm thick copper plates. Copper pipes, carrying cooling water, were glued to these plates to provide thermal stabilisation for the crystals. Two thermal sensors were installed on either side of the crystal assembly, providing a temperature monitoring precision better than 0.1 °C. The temperature variation was found to be lower than 0.2 °C and its effect on the system stability was negligible.

An LED-based system, similar to the one used in EE, has been used for monitoring the crystal transparency. It consisted of a blue LED light source (455 nm emission peak) and a bundle of quartz optical fibres used to deliver the light to the back end of each crystal. The photon flux was not sufficient to produce optical annealing and thus it did not bring changes to the optical transmission of the crystals. The complete module, including the cooling and light monitoring system, was mounted inside a sealed aluminium box, which provided optical and thermal isolation. The box was installed on a remotely-controlled $x - y$ table with a displacement range of ± 30 cm and positioning precision of ∼ 1 mm. Figure 7 shows a photograph of the setup used in the H4 beam tests of irradiated crystals.

2016 JINST 11 P04012

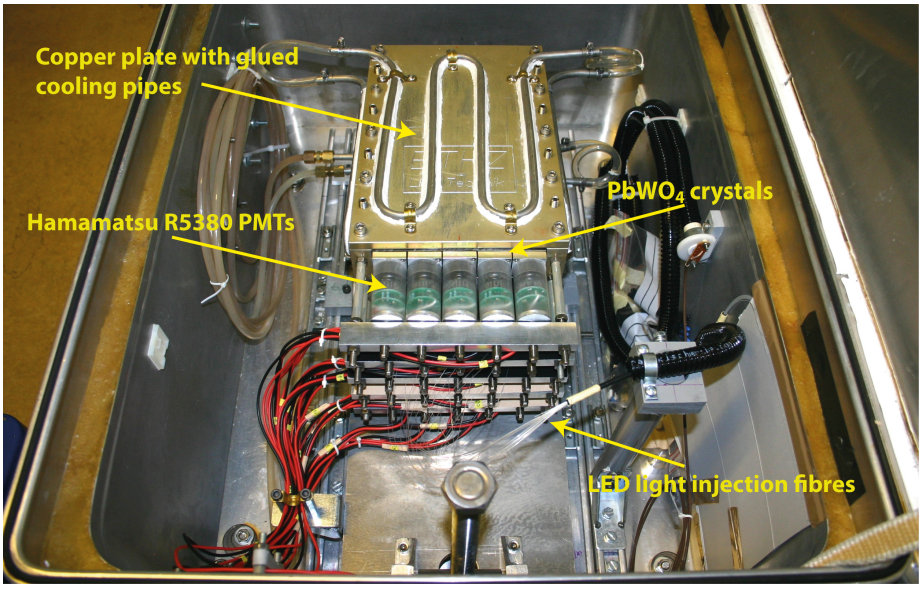

Figure 7. Photograph of the setup used in the H4 beam tests of irradiated crystals.

3.2 Crystal matrix configurations

The crystals inside the test module were arranged in 5×5 matrices configured to have the irradiated crystals placed within the central 3×3 array, surrounded by non-irradiated or slightly-irradiated crystals. Figure 8 shows the six 5×5 matrices used in 2011 and 2012. The values of $\mu_{\rm ind}$ quoted for each crystal in this figure represent the average $\mu_{\rm ind}$ measured just before the beam tests.

As discussed in section 4.3, to reconstruct the energy deposited by electron showers, limiting transverse leakage, a matrix made of 3×3 crystals has to be used. Since the matrices of crystals used for this study are characterized by different values of $\mu_{\rm ind}$, we define an average $\mu_{\rm ind}^{3\times3}$ of the matrix by weighting the $\mu_{\rm ind}$ of each crystal with its relative contribution to the reconstruction of an electromagnetic shower centered on the 3×3 matrix:

$$\mu_{\rm ind}^{3\times3} = \sum_{i=1}^{9} \mu_{\rm ind}^{i} \cdot w^{i} \tag{3.1}$$

where for the central crystal, w^5 is equal to 0.84; for the crystals adjacent to the central one $w^2 = w^4 = w^6 = w^8 = 0.032$; and for the crystals in the corners of the matrix $w^1 = w^3 = w^7 = w^9 = 0.008$. The weights have been determined by measuring the average fraction of energy deposited in each crystal of the 3×3 non-irradiated matrix using 50 GeV electrons located within a 10×10 mm^2 beam spot. The values of the weights are the same, within systematic uncertainties, for the energy range considered in this analysis (10–150 GeV).

During the 2011 beam-test period a matrix of proton-irradiated crystals with different $\mu_{\rm ind}$ in the range from 0 to 11 m^{-1} was tested. Some of the crystals were partially annealed, prior to the beam tests, by heating them to 300°C for several hours after irradiation. The values of $\mu_{\rm ind}$ shown in figure 8 correspond to the induced absorption measured just before the beam test. The responses of two clusters centered around crystals 11 and 12 have been analyzed. The average $\mu_{\rm ind}^{3\times3}$ of these highly non-uniform clusters is 10.1 m^{-1} and 3.5 m^{-1} respectively.

2016 JINST 11 P04012

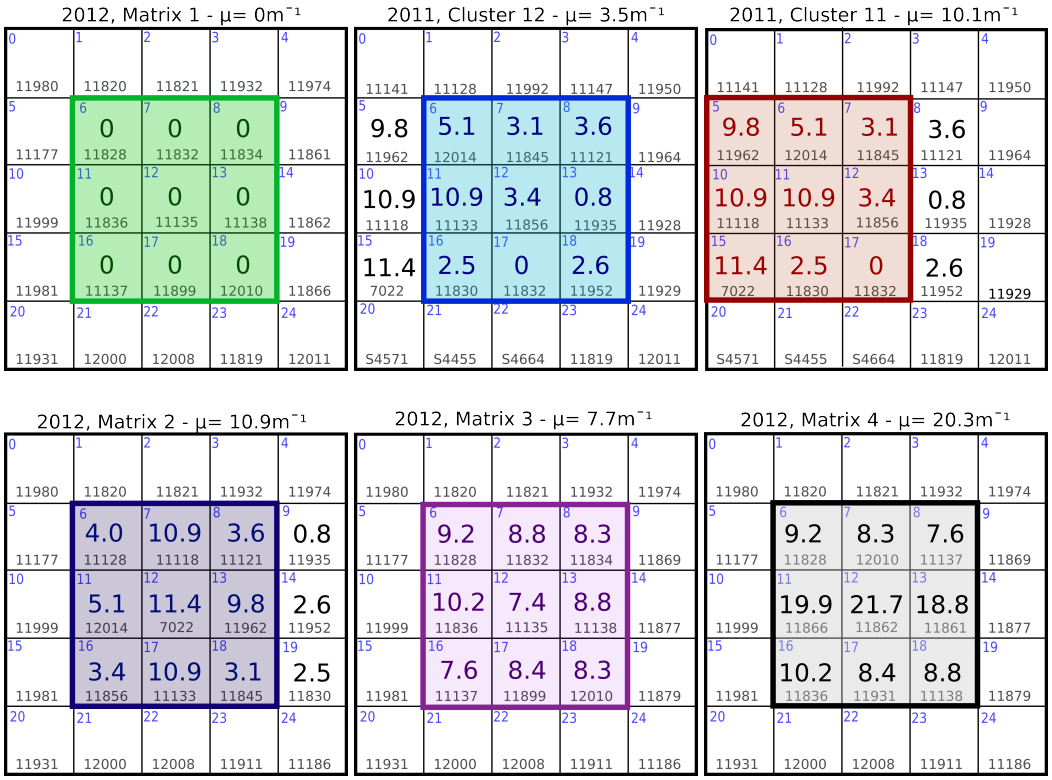

Figure 8. Set of proton-irradiated matrices used for the test beam. The numbers in bold represent the μ_{ind} of each crystal. The numbers at the top represent the position of the crystal in the alveolar structure and those at the bottom are the unique identification numbers of the corresponding crystal. The heading for each matrix also includes the weighted average of the μ_{ind} for the corresponding 3×3 central crystals.

During the 2012 test beam period, three matrices of proton-irradiated crystals have been tested. Matrix 2 was made of crystals that were damaged and partially recovered during 2011, whereas matrices 3 and 4 were made of crystals that had been irradiated in July 2012 to proton fluences between 5.3×10^{13} cm^{-2} and 1.3×10^{14} cm^{-2}. The values of induced absorption (μ_{ind}) for the crystals used in the matrices studied during 2012 cover the range 0 to 22 m^{-1}, essentially the full spread of μ_{ind} expected between LHC startup and the end of the HL-LHC phase at the highest pseudorapidity.

3.3 The beam line infrastructure

The incoming electrons from the H4 beam line at the CERN SPS North Area were detected by a set of four scintillation counters used to trigger the data acquisition. The impact of the beam particles on the crystal matrix was measured using two sets of beam hodoscopes. Each set comprised two orthogonal planes of 64 scintillating fibres with square cross-section 0.5×0.5 mm^2, read out by a multi-anode PMT. Each plane provides, respectively, a measurement of the electron position in the x and y directions with a nominal precision better than 200 μm [24]. The signals from the PMTs, beam counters and hodoscopes were delivered to the counting room, located about 60 m from the beam zone, by coaxial cables and digitized by a 12-bits VME LeCroy Charge Analog-to-Digital Converter (ADC) [25]. The integration time was set to 300 ns to accommodate the PMT pulse

2016 JINST 11 P04012

length and channel-to-channel transition time variation in the long coaxial cable connecting PMT output and ADC input.

3.4 Experimental procedure

The bias voltage of the crystal PMTs was turned on about one week before the start of the beam test. The DAQ ran continuously during this period, acquiring LED monitoring data as well as pedestal (PED) events. The LED monitoring data provided a measurement of the PMT gain variation with time, assuming that the transparency of crystal remains unchanged during data taking. The LED signal was found to be stable to better than 1%. After the beam start-up, the bias voltage of each PMT was calibrated such that the peak signal from a 50 GeV electron shower corresponded to about 1500 ADC counts in each crystal. This setting allowed the use of the same PMT gain for the entire electron energy scan in the range 10–150 GeV.

Calibration of the crystal matrix readout chain was performed by positioning the crystals, one-by-one, into the 50 GeV electron beam by moving the table that supported the matrix. The trigger was defined as the coincidence of scintillator signals, providing a beam spot of about 10×10 mm^2. The table movement was controlled by the same PC that ran the data acquisition software. The calibration procedure was fully automatic such that, for standard beam conditions, the full matrix calibration required about 60 minutes, during which time about 50k events were collected for each crystal.

After calibration, energy scans were performed with the beam centered on the central crystal of each matrix. The configuration of the H4 beam line provided an electron beam in the momentum range 10 GeV/c to 150 GeV/c with hadron and muon contamination below 0.2% and small angular divergence. Beam momenta of 10, 20, 50, 100, 120 and 150 GeV/c were used. The momentum resolution of the beam line, defined by the collimators and magnets, was set to the optimal value for H4 of about $\delta(p)/p = 0.3\%$, where $\delta(p)$ is the FWHM of the momentum distribution.

3.5 Simulation framework

A simulation framework was developed in order to understand the effects of radiation damage on the crystal performance. The Geant4 software [27], simulating the electron shower development inside the $PbWO_4$ crystal matrix, was combined with the ray-tracing software SLitrani [28]. This combined framework was used to simulate the scintillation process and the subsequent light propagation through the crystal volume, including reflection and absorbtion. Photons exiting the rear face of the crystal then pass through a layer of grease (refrative index 1.45). Photons are "detected" if they then enter a volume with the same size and geometry as the PMTs. The crystal scintillation properties, as described in [2], have been used and representative values of $\mu_{\rm ind}$ (from 0 to 30 m^{-1}) were simulated. The results obtained were compared with the experimental data and are discussed in section 5.

4 Analysis

4.1 System stability and noise

The LED light injection system and daily calibration of the full matrices, using 50 GeV electrons, were used to monitor the stability of the PMT+crystal+electronics chain response. We found the system to be stable to the level of ~1% during the whole test beam period.

2016 JINST 11 P04012

The channel pedestals were continuously monitored. Both the mean pedestal value and σ_{ped} were estimated by fitting the pedestal distribution with a Gaussian function. The pedestal means have been subtracted from the signals, channel-by-channel, to obtain the signal amplitudes. The σ_{ped} values have been used to estimate the contributions of the channel noise to the energy resolution. Channel-dependent equivalent noise values between 40 and 150 MeV were found.

The noise contribution, B (in GeV), to the reconstructed energy resolution when using a 3×3 cluster of crystals has been calculated by adding in quadrature the weighted contributions of the σ_{ped} (in ADC counts) for each channel involved in the reconstruction:

$$B = G \cdot \sqrt{\sum_{i=1}^{9} (\sigma_{\text{ped}}^{i} \cdot IC_i)^2} \tag{4.1}$$

where G is the global ADC to GeV conversion factor, IC_i are the intercalibration coefficients for channel i, which allows the different gain of each PMT and the crystal light output to be taken into account (see section 4.3) and σ_{ped}^{i} is the σ of the pedestal corresponding to a specific channel. Eq. 4.1 is valid only if there is no correlated noise between the channels. No correlation between channels was found.

The total noise, $\sigma_{\text{ped}}^{3\times3}$, for the 3×3 central matrices examined in 2011 and 2012 varied between 170 MeV and 340 MeV. This difference was mainly due to different bias voltages used for the PMTs in different periods. The appropriate noise value was used in the calculation of the energy resolution for that matrix.

4.2 Beam spot selection

The beam hodoscopes were used to reconstruct the impact point on the crystal by extrapolating the electron trajectory. The response of a particular crystal varies with impact point due to the variation of containment of the energy deposited in the crystal, given that the crystal transverse dimensions (3×3 cm^2) are of the same order as the Molière radius of $PbWO_4$ (≃2.2 cm). The centre of the crystal is defined as the position where the maximum response is observed. This maximum is obtained from a fit to the measured response profiles using a 2nd-order polynomial. The centre of the matrix is determined with ∼1 mm precision in x and y for non-irradiated crystals (see figure 9).

Applying the same method to the irradiated matrices of 2012, we observed irregular containment distributions, as shown in figure 10. This leads to a biased estimation of the crystal centre. These irregularities are due to transverse non-uniformities of the damage inside the crystals. For the three irradiated 2012 matrices, the same coordinates of the centres were used (as extracted from the non-irradiated matrix), since the position of the box was maintained with 1 mm precision. In the range of ±5 mm from the centre of the crystal, corresponding to the beam spot selection used in this analysis, the non-uniformity of damage causes a variation of response at the level of ∼ 1.5%. This is comparable to the change of response due to containment, as measured for non-irradiated crystals in figure 9.

Figure 11 shows the calibrated summed energy distributions for 50 GeV electrons observed in three matrices in 2012. The two histograms in each plot are for different beam-spot selections: the red histograms were obtained using a 10×10 mm^2 selection around the centre of the crystal; the black histogram used a 4×4 mm^2 selection. The distributions, including the peak widths, are

2016 JINST 11 P04012

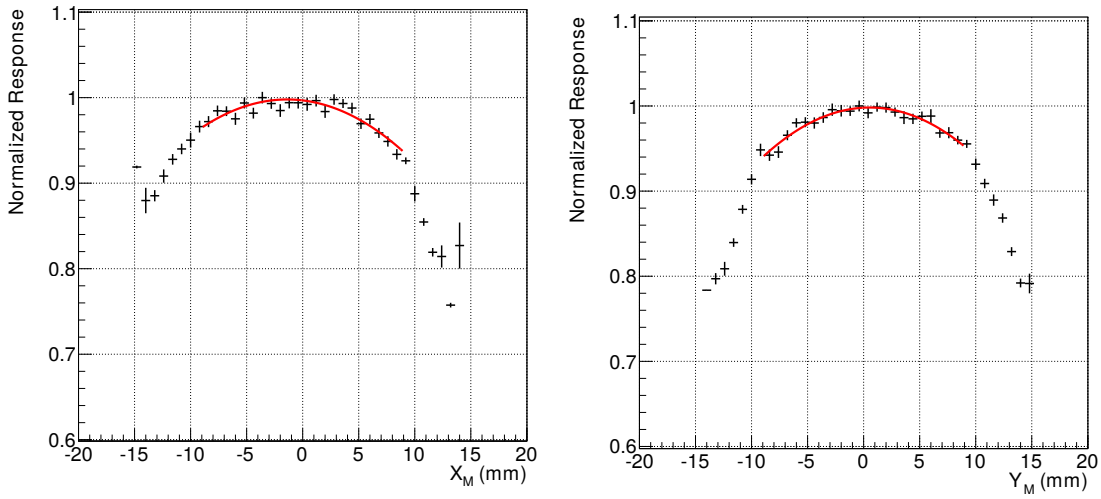

Figure 9. The profiles of the crystal response with respect to the impact point normalized at the maximum, shown separately for x and y axes in the matrix coordinate system. A 2nd order polynomial fit is performed in the range ±10 mm to find the maximum, which is assumed to be the centre of the crystal. The plots correspond to the central crystal of the non-irradiated matrix in 2012.

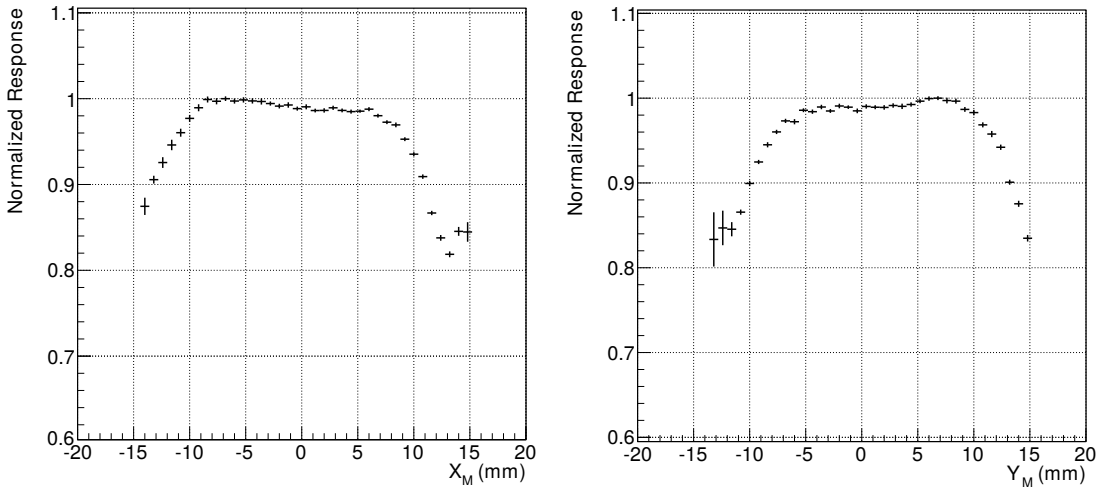

Figure 10. The profiles of the crystal response with respect to the impact point normalized at the maximum, shown separately for x and y axes in the matrix coordinate system. These distributions, obtained from central crystal of the irradiated matrix 3 in 2012, are not symmetric and their maximum does not correspond precisely to the centre of the crystal.

comparable for the two beam-spot selections. The larger spot size was preferred due to the higher statistics obtained. An even larger selection could have been used, but in this case systematic effects due to transverse non-uniformity of the damage would have become significant.

2016 JINST 11 P04012

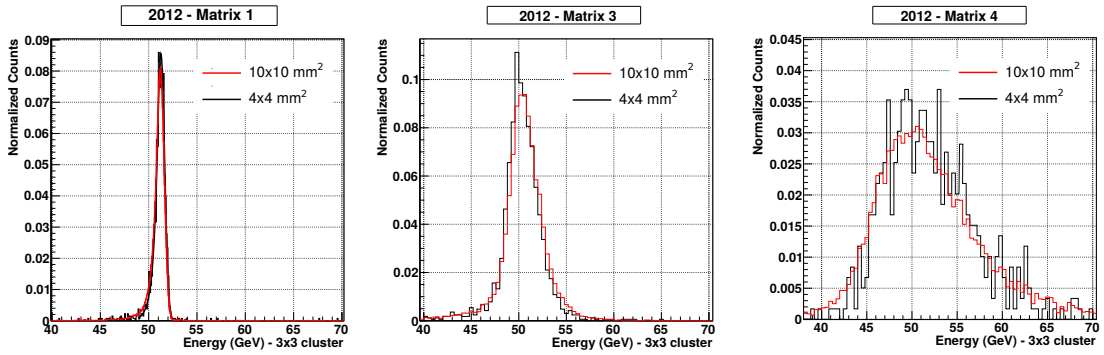

Figure 11. Amplitude distributions reconstructed using a 3×3 cluster with a 50 GeV electron beam, with a beam spot selection of 4×4 mm^2 (black) and 10×10 mm^2 (red). From left to right the distributions corresponding to clusters centered around the central crystal for matrices of 2012 are shown, matrix 1 ($\mu_{\rm ind} = 0$ m^{-1}), matrix 3 ($\mu_{\rm ind}^{3\times3} = 7.7$ m^{-1}) and matrix 4 ($\mu_{\rm ind}^{3\times3} = 20.3$ m^{-1}).

4.3 Calibration

The calibrated amplitude of the signal in an individual channel, E_i (in ADC counts), is defined as:

$$E_i = IC_i \cdot R_i \tag{4.2}$$

where R_i is the signal in ADC counts from channel i. The intercalibration coefficients IC_i were obtained for all crystals during calibration runs and vary between 1 and 2.5. To calculate these coefficients, the ADC-count distribution obtained for each crystal from 50 GeV incident electrons, after the beam spot selection, has been fitted using a Crystal Ball function [29, 30]. The inverse of the peak position obtained from the fit, normalized to a reference value, yields the intercalibration coefficient for the corresponding channel. The precision on these coefficients was estimated to be around 0.2%.

Once the individual channels have been intercalibrated, the energy in GeV deposited by the shower within a 3×3 cluster of crystals can be estimated by summing-up the contributions from the 9 channels and applying an overall ADC-to-GeV conversion factor:

$$E_{3\times3} = G \cdot \sum_{i=1}^{9} E_i \,. \tag{4.3}$$

The ADC-to-GeV calibration coefficient, G, of eq. (4.3) is obtained by setting the peak (from a Crystal Ball fit) of the energy reconstructed using the 3×3 matrix to be equal to the beam energy. It follows that for each channel, general ADC-to-GeV calibration coefficients $G_i = G \cdot IC_i$ can be obtained to include the intercalibration coefficients as used in eq. (4.1).

4.4 Energy linearity

The matrices have been exposed to electron beams with energies between 10 and 150 GeV. The energy linearity, $L(E_{\rm b})$, has been defined as the ratio between the reconstructed energy, $E_{3\times3}$, and the nominal beam energy $E_{\rm b}$:

$$L(E_{\rm b}) = \frac{E_{3\times3}}{E_{\rm b}} \,. \tag{4.4}$$

2016 JINST 11 P04012

By definition $L(E_b)$ is equal to unity for $E_b = 50\,\text{GeV}$, which is the energy used to calibrate the reconstructed response.

The PMT response non-linearity, as stated by the producer [23], is lower than 1% for the peak output current of 10 mA. This current corresponds to the maximum for the 150 GeV electron signal. The ADC is linear at the level of ± 0.25% within the full measurement range [25]. Since non-linearities in the readout chain response are the same for each crystal, they cancel out when considering the differential non-linearity as discussed in section 5. Our analysis focuses on the changes in linearity of the crystal response with radiation damage.

4.5 Energy resolution

The standard parameterization of the calorimeter energy resolution, $\frac{\sigma_E}{E}$, has been used in this analysis:

$$\frac{\sigma_E}{E} = \sqrt{\left(\frac{A}{\sqrt{E}}\right)^2 + \left(\frac{B}{E}\right)^2 + C^2} \tag{4.5}$$

where A represents stochastic fluctuations, C is the constant term and B is the contribution due to electronic noise. The value of B is estimated for each matrix configuration using the corresponding noise found from pedestal events. To disentangle the contribution of the noise to the resolution of a given matrix, the noise B has been subtracted in quadrature from the $\sigma(E)/E$ for each matrix.

Even when using the tight 4×4 mm^2 beam spot selection, the energy distributions of both irradiated and non-irradiated crystals show asymmetric tails. This is shown in figure 12 for crystal 11135 before and after irradiation to a μ_{ind} of 7.4 m^{-1}, both for the single crystal and 3×3 matrix sum centered on this crystal. In particular, a low energy tail is observed for non-irradiated matrices while a high-energy tail appears for highly-irradiated ones. The occurrence of the high-energy tail for crystals irradiated in 2011, having a flat transverse damage profile, suggests that this asymmetry is not related to transverse non-uniformity of 2012 irradiated crystals, but to the intrinsic non-uniformity of light collection inside the crystals due to their tapered shape.

To take into account the asymmetries in the energy distributions, we define σ_{eff} as half of the minimum interval containing 68% of the $E_{3\times3}$ distribution. This quantity is used in the following analysis as an estimate of the energy resolution:

$$\frac{\sigma(E)}{E} = \frac{\sigma_{\text{eff}}(E)}{E} \tag{4.6}$$

where E is the value obtained from a Crystal Ball fit corresponding to the most probable value of the $E_{3\times3}$ distribution.

5 Results

Our analyses concentrated on measurements of the radiation-dependent response degradation and consequent worsening of the energy resolution and energy linearity. In most cases we used 3×3 matrices of crystals, but begin by studying the response degradation for single crystals.

2016 JINST 11 P04012

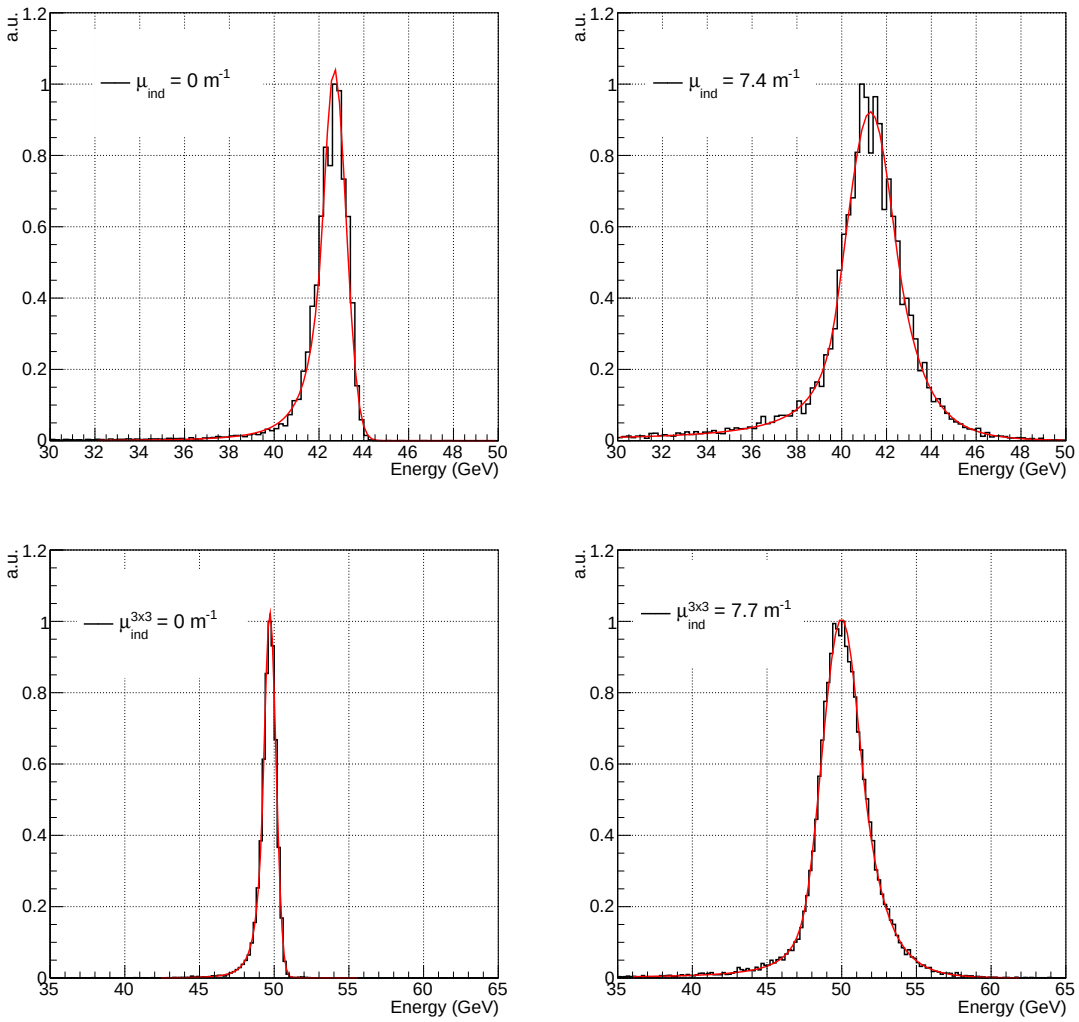

Figure 12. Top: single crystal 50 GeV electron energy spectra for crystal 11135 before (left) and after (right) irradiation to a $\mu_{\rm ind}$ = 7.4 m^{-1}. Bottom: 3×3 cluster of non-irradiated crystals in the 2012 matrix 1 ($\mu^{3\times3}_{\rm ind}$ = 0 m^{-1}) centered on crystal 11135 (left) and the 3×3 cluster of irradiated crystals in the 2012 matrix 3 ($\mu^{3\times3}_{\rm ind}$ = 7.7 m^{-1}) centered on the same crystal (right). Note that the crystals used in the 3×3 arrays used in 2012 matrix 1 and 3 are the same. A beam spot selection of 4×4 mm^2 has been applied to reduce shower containment effects.

5.1 Single crystal light output

To estimate the crystal light output (LO) loss due to proton irradiation we compared the 50 GeV electron peak position, $R_{i(\rm ni)}$, for irradiated and non-irradiated crystals. In each comparison we used the same PMT with the same HV settings and same beam spot definition. In the case of the crystals irradiated in 2012 and used in the 2012 matrices 3 and 4, a direct before/after comparison could be made as they were tested in the beam before/after irradiation. The crystals used in 2012 matrix 2 were not tested in the beam before irradiation so we compared with non-irradiated crystals with similar light outputs (within 5–8%). For these crystals we defined LY_1 as the light yield (LY)

2016 JINST 11 P04012

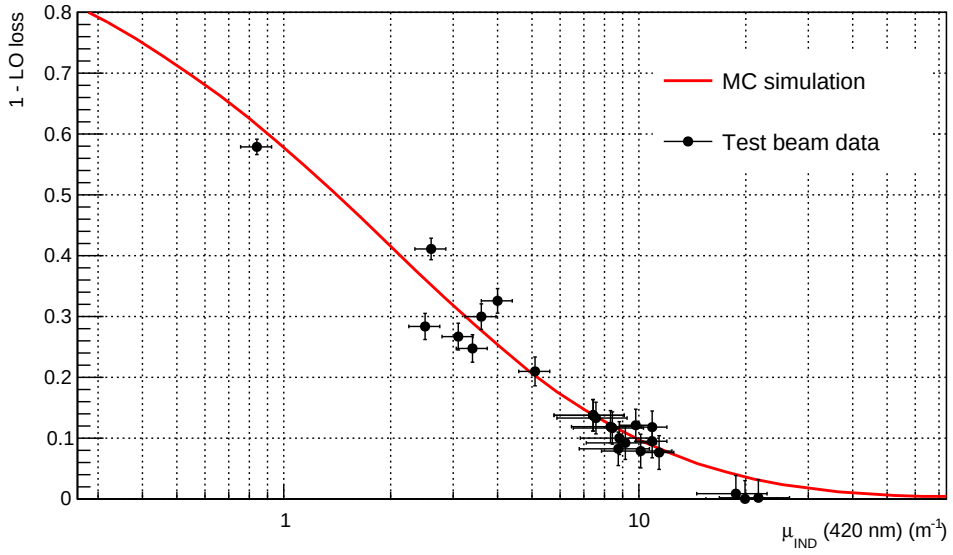

Figure 13. Light output loss as a function of the induced absorption coefficient μ_{ind} for matrices tested in beams in 2012. The red line shows the prediction from the GEANT4+SLitrani simulation.

of the reference non-irradiated crystal and LY_2 as the LY of the irradiated crystal before irradiation. We then define the light output loss as:

$$\text{LO}_{\text{loss}} = \frac{R_{\text{ni}} - R_i \cdot \frac{LY_1}{LY_2}}{R_{\text{ni}}} . \tag{5.1}$$

The correction $\frac{LY_1}{LY_2}$ is applied to take into account the difference in the light yield between the two crystals. This correction contributes to the systematic uncertainties due to the 5% precision of the light yield measurement.

The results are shown in figure 13 and compared with the GEANT4+SLitrani simulation. The simulation matches rather well the data, over a wide range of μ_{ind} and LO loss. The amount of signal remaining after severe irradiation, with μ_{ind} greater than 10 m^{-1}, is very small, around 10% or less than the non-irradiated signal.

The systematic error of this measurement has been estimated by examining the light output of several non-irradiated crystals, which by definition have zero LO loss. The spread of the values around 0 is about 3%. This systematic error dominates the statistical error due to the fitting procedure ($\sim$ 0.1%). This uncertainty is also much larger than the systematics due to non-uniform damage in 2012-irradiated crystals. Measurements of LO loss for highly irradiated crystals are less precise since the signal to noise ratio is smaller, as shown in figure 14.

The average μ_{ind} calculated for 2012 crystals represents a lower limit of the effective μ_{ind} that can affect the propagation of scintillation photons. This is due to the fact that the selected electron showers are located predominantly close to the central region of the crystal where the damage is highest. This explains the non-uniform containment profiles reported in figure 10. The effect of transverse damage non-uniformity to the measurement of light output was estimated to be 1.5%.

2016 JINST 11 P04012

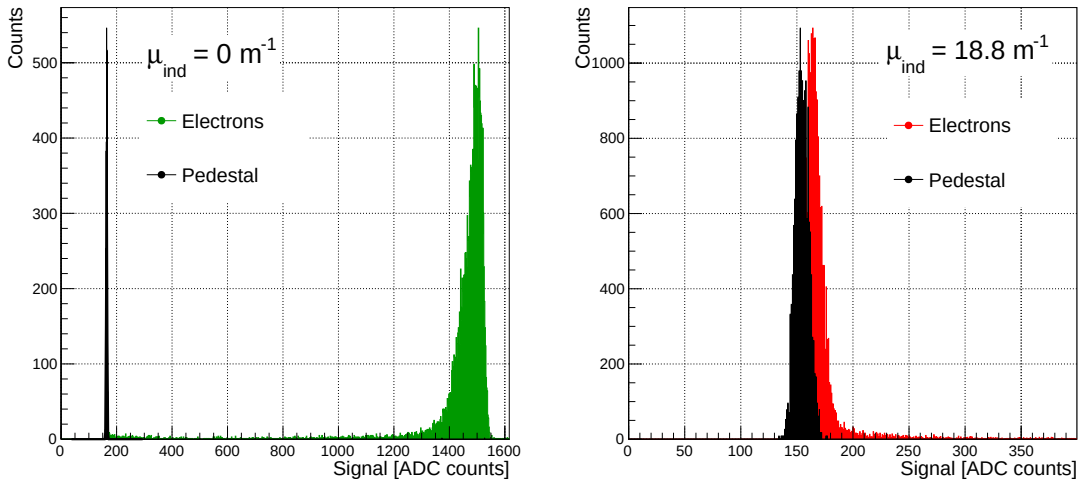

Figure 14. Left: ADC spectrum of a 50 GeV electron beam for crystal 11861 before irradiation. Right: ADC spectrum obtained for the same crystal after proton irradiation ($\mu_{\text{ind}} = 18.8\ \text{m}^{-1}$). In both cases the black peak at low ADC values represents the pedestal.

5.2 Non-irradiated matrix performance

During 2012 test beams, a 5×5 matrix of non-irradiated crystals has been characterized with electrons to evaluate energy linearity and resolution with the PMT+electronics chain used for subsequent measurements of irradiated crystals. To estimate the systematic error of these measurements we computed the linearity and the resolution of all nine 3×3 clusters centered around each of the nine central crystals. The average resolutions and linearities of these matrices were used as the best estimations for non-irradiated crystals and the envelope was used to estimate the respective uncertainties. The results are presented in figure 15.

A stochastic term of $6.8 \pm 0.9\%$ is obtained from the fit of the energy resolution curve in figure 15. This is consistent with previous beam-test measurements of endcap crystals [2]. The response of the non-irradiated matrices to electrons of 10–120 GeV energy is linear within the experimental uncertainty of $\sim 1\%$.

5.3 Performance of irradiated matrices

A comparison between the performance of irradiated matrices presented in section 3 has been performed. The non-linearity of the response of the matrices has been studied as a function of $\mu_{\text{ind}}^{3\times3}$ and the degradation of resolution due to the change of transparency/uniformity of damaged crystals has also been investigated.

5.3.1 Response non-linearity

Figure 16 (left) shows the linearity, $L(E_{\text{b}})$ (defined in section 4.4), as a function of beam energy for crystal matrices with different average induced-absorption coefficients ($\mu_{\text{ind}}^{3\times3}$). The irradiated crystals show increasing non-linearity as μ_{ind} increases. This can be interpreted as the effect of transparency loss on the uniformity of light collection efficiency ε_{LC} along the crystal length. As

2016 JINST 11 P04012

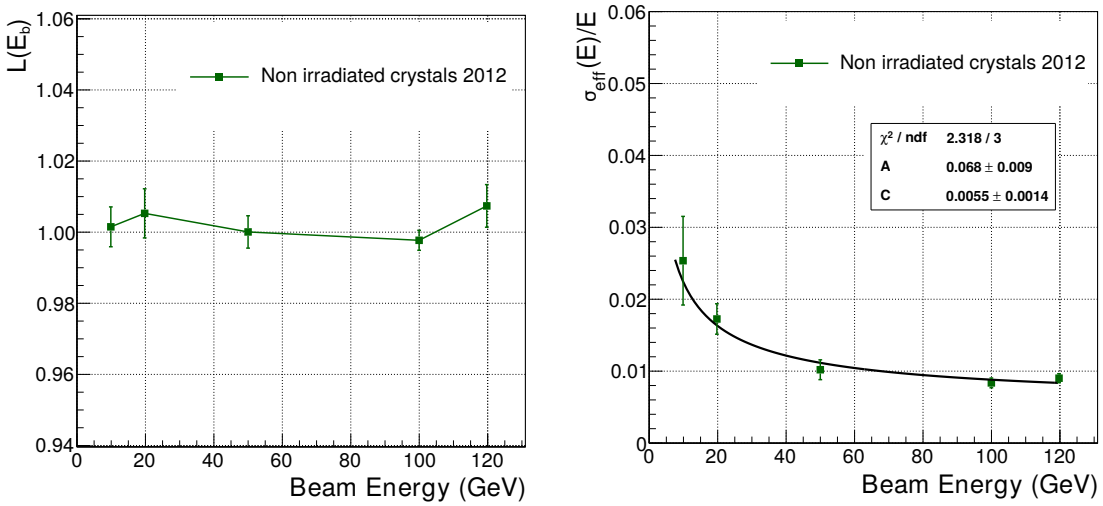

Figure 15. Average linearity (left), defined as $\frac{E_{3\times3}}{E_{\text{beam}}}$, and energy resolution (right) for the 3×3 clusters of non-irradiated crystals centered on the nine central crystals of 2012 matrix 1.

the μ_{ind} reaches similar values to the inverse crystal length, photons produced far from the PMT will have lower average probability to be detected than those produced close to the PMT. This probability, ε_{LC}, can be approximated by:

$$\varepsilon_{\text{LC}} \approx K \cdot e^{-\nu(\mu_{\text{ind}})\cdot D} \tag{5.2}$$

where K is the average probability for a photon produced very close to the photodetector (at a distance $D = 0$) to be detected and $\nu(\mu_{\text{ind}})$ is a positive attenuation coefficient that increases with larger μ_{ind}. From eq. (5.2) it can be deduced that higher values of μ_{ind}, i.e. higher values of $\nu(\mu_{\text{ind}})$, result in larger non-uniformities because the exponential curves become steeper.

The position t_{max} of the electromagnetic shower maximum moves towards the rear face of the crystal with higher energy according to:

$$t_{\text{max}} \propto \ln\left(\frac{E_{\text{b}}}{E_{\text{c}}}\right) \tag{5.3}$$

(with critical energy $E_{\text{c}} = 7.94\,\text{MeV}$ for $PbWO_4$). As a consequence, the light produced by low-energy showers is more suppressed by the transparency loss since the average path to reach the photodetector is longer. The light attenuation along the crystal introduces a non-linear effect on the energy reconstruction. For each energy E_{b} of the incoming electron, the exact effect of the μ_{ind} on the non-linearity of the measured signal can be estimated by convolving the longitudinal profile of shower development with the light collection efficiency curve ε_{LC}. To first approximation, eq. (5.2) and (5.3) suggest a parameterization of the linearity L as follows:

$$L(E_{\text{b}}) = L_0 + \exp\left[S_{\text{NL}} \cdot \ln\left(\frac{E_{\text{b}}}{E_{\text{c}}}\right)\right] \tag{5.4}$$

where S_{NL} is a non-linearity parameter related to μ_{ind} and L_0 is an offset which takes into account the arbitrary normalization at 50 GeV. Using eq. (5.4), in which L_0 and S_{NL} are free parameters, the

2016 JINST 11 P04012

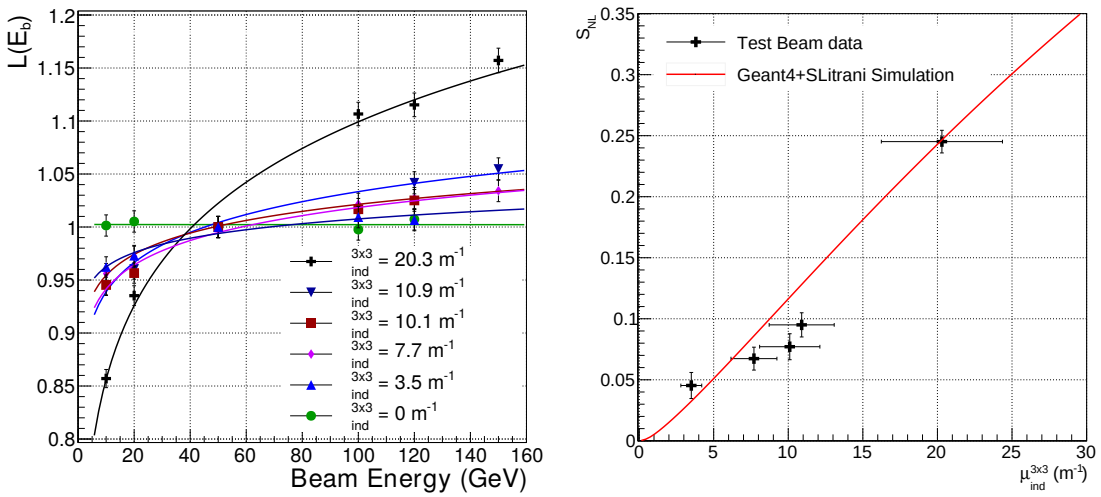

Figure 16. Fit of linearity curves for the 2012 and 2011 irradiated matrices (left) and comparison of non-linearity for different values of $\mu_{\rm ind}^{3\times3}$ with predictions from simulation (red line, right plot).

linearity curves obtained from irradiated matrices have been fitted and the values of $S_{\rm NL}$ estimated. A good agreement between the value of $S_{\rm NL}$ predicted by simulation for a given $\mu_{\rm ind}^{3\times3}$ and the beam-test measurements is observed, as shown in the right plot of figure 16.

Two important aspects are involved in the energy reconstruction with a 3×3 cluster of crystals: firstly, each crystal has a different $\mu_{\rm ind}$, which means a different non-linear response to the fraction of energy deposited in it; secondly, the signal in the surrounding crystals of a given cluster may be very close to the pedestal, for low energy runs (10 and 20 GeV) and for highly irradiated crystals in particular. To understand whether these aspects could bias the energy reconstruction, the linearity of response has been calculated using only the central crystals of the matrices. In this case, to cancel out the effects due to partial containment of the shower, the differential non-linearity, $L^*(E_{\rm b})$, defined as the ratio of linearity of an irradiated crystal to the linearity of a non-irradiated one, was used. The comparison for matrices 3 and 4 of 2012 is shown in figure 17. The linearity curves are similar to those of the corresponding 3×3 matrix within the uncertainty. The difference observed for matrix 4 crystals can be attributed to the difference between the corresponding induced absorption coefficient of the cluster, $\mu_{\rm ind}^{3\times3}$, with the respect to the one of the central crystal, $\mu_{\rm ind}^{\rm c}$.

5.3.2 Energy resolution degradation

The energy resolution calculated for each matrix is shown in the left plot of figure 18. Fits have been performed in order to extract the stochastic and constant terms. The fit parameters (using eq. (4.5)) are reported in table 2. For irradiated crystals and for typical electron/photon energies of interest — above ~40 GeV — the constant term dominates the energy resolution.

In this test beam configuration several contributions affect the constant term: the different $\mu_{\rm ind}$ of the crystals within a 3 × 3 cluster, the partial containment of the shower inside a limited-size matrix and the non-uniformity of light collection efficiency along a single crystal. The plots of figure 18 show that the constant term evolves from 0.55% for non-irradiated matrices to 10.3% for

2016 JINST 11 P04012

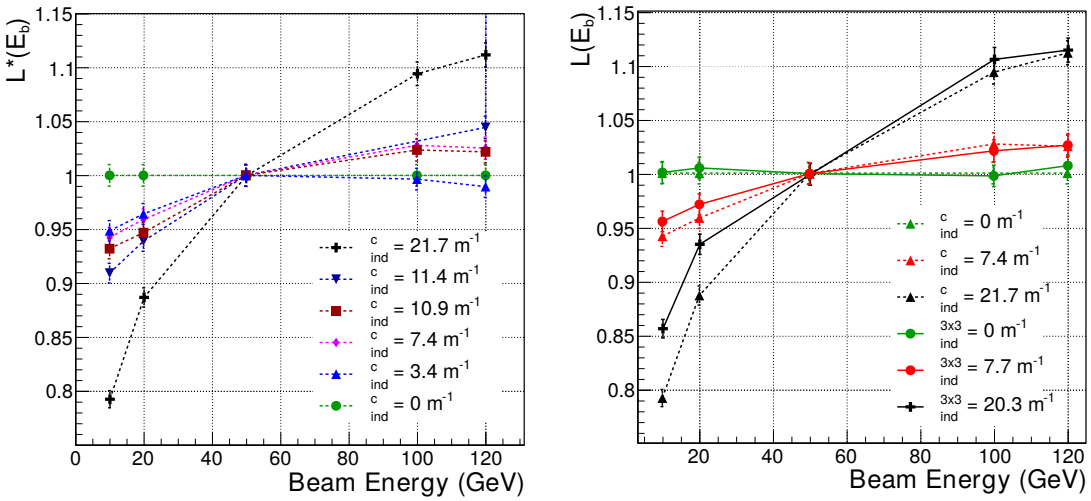

Figure 17. Left: linearity curves for central crystal only. Right: comparison of linearity for 3×3 clusters with the linearity of the corresponding central crystals for 2012 matrices 3 and 4.

Table 2. Stochastic and constant terms extracted from the fits to the energy resolution as a function of energy for each matrix.

Matrix	$\mu_{\text{ind}}^{\text{central}}$ (m^{-1})	$\mu_{\text{ind}}^{3\times3}$ (m^{-1})	A (% GeV$^{1/2}$)	C (%)
2012 — 1	0.0	0.0	6.8 ± 0.9	0.5 ± 0.1
2011 — 1	3.4	3.5	8.9 ± 0.6	2.3 ± 0.2
2012 — 3	7.4	7.7	12.7 ± 1.0	3.1 ± 0.2
2011 — 2	10.9	10.1	11.8 ± 0.8	3.7 ± 0.2
2012 — 2	11.4	10.9	12.5 ± 1.4	4.9 ± 0.3
2012 — 4	21.7	20.3	24.5 ± 3.0	10.3 ± 0.5

the most damaged matrix tested in 2012. To estimate the change in the constant term ΔC induced by the damage and hence related to an increase of ε_{LC} non-uniformity, we subtracted the constant term of a non-irradiated matrix C_{ni} from the values of irradiated matrices C_i according to:

$$\Delta C = \sqrt{C_i^2 - C_{\text{ni}}^2} \tag{5.5}$$

and compared the result with the $\mu_{\text{ind}}^{3\times3}$ of the corresponding cluster. A good correlation is observed between the increase of the constant term and the value of $\mu_{\text{ind}}^{3\times3}$. The good agreement of simulation with experimental observation of the constant term degradation in figure 18 is a validation that the simulation model can well reproduce the mechanisms of performance degradation due to loss of transparency and uniformity in the crystal.

5.4 Change in scintillation pulse shapes

During the 2011 test beam period, the measurement of the waveform of the pulse generated by a 50 GeV electron shower inside $PbWO_4$ crystals was also performed. For this measurement,

2016 JINST 11 P04012

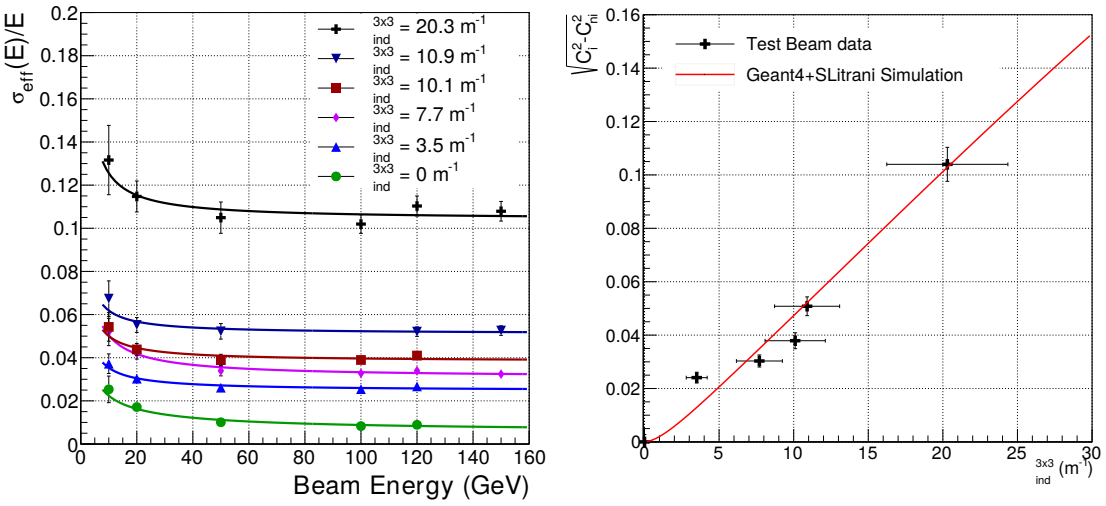

Figure 18. Left: the resolution at different energies is compared for different matrices. Right: experimental correlation between the constant term degradation due to non-uniformity of light collection and the corresponding $\mu_{\text{ind}}^{3\times3}$ compared with prediction of simulation.

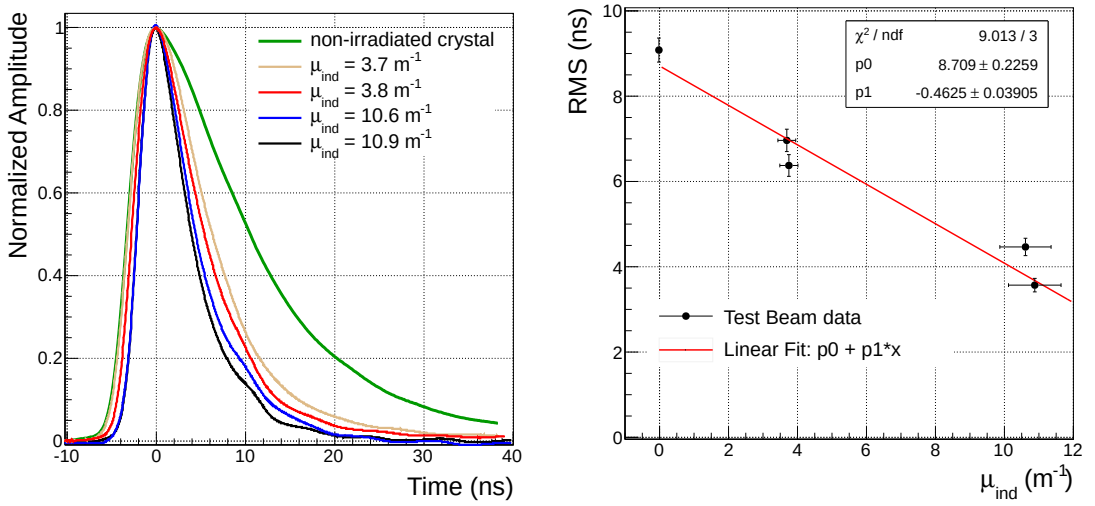

Figure 19. Left: waveforms of a non-irradiated crystal and four proton-irradiated crystals are shown. The μ_{ind} of the irradiated crystals varies between 3.7 m^{-1} and 10.9 m^{-1}. Right: correlation between μ_{ind} and RMS of the average pulse fitted with a linear function (red).

the PMT outputs were connected to an Agilent DSO90254A 2.5 GHz oscilloscope using 20 m high-bandwidth coaxial cables. A thousand pulse waveforms were recorded for each crystal.

The average waveforms, normalized to the amplitude, of a non-irradiated crystal and four proton-irradiated crystals are presented in figure 19. The pulses from the damaged crystals are almost twice as fast, which can be attributed to the shorter average path of the scintillation photons due to the lower light transmission of the damaged crystals. A correlation between the μ_{ind} of a given crystal and the RMS of its average waveform is shown in the right plot of figure 19.

2016 JINST 11 P04012

6 Conclusion

The results presented in this paper show the performance of CMS ECAL endcap-like modules, constructed from 5×5 proton-irradiated $PbWO_4$ crystals, in terms of light output, energy linearity, energy resolution and pulse shapes. The tested modules were made of $PbWO_4$ crystals with different levels of proton-induced damage up to an induced absorption coefficient μ_{ind} of 21.7 m^{-1} for a fluence of 1.3×10^{14} p/cm^2. Independent measurements of μ_{ind} for crystals irradiated in situ in CMS show no significant dose-rate dependence on the damage. Assuming no annealing of the proton damage at room temperature, such induced absorption coefficients are expected to represent the effect of the hadron fluences predicted for the ECAL Endcaps (at $|\eta| = 2.6$) up to an integrated luminosity of ~3000 fb^{-1}.

The data collected during several beam-test periods, performed at the H4 facility at CERN, have been analyzed and compared. Several important effects have been observed. The light output significantly decreases due to transparency loss of the irradiated crystals. In addition, the detected scintillating pulses of crystals become faster as μ_{ind} increases.

Using electrons in the 10–150 GeV energy range, the response of 3×3 matrices of crystals has been investigated. A non-linearity of the energy reconstructed using irradiated matrices has been observed. In addition, we found that the constant term increases from ~ 0.55% to ~ 10% with the fluences explored and dominates the energy resolution. The experimental results have been compared with a Geant4 + SLitrani simulation and showed good agreement. Other effects, such as a variation in the shape of the amplitude distribution of reconstructed energy, have also been observed.

The study presented in this paper proves that the main effects of the proton radiation damage in $PbWO_4$ crystals can be understood and described, to a first approximation, in terms of the (non uniform) light transmission loss inside the crystal. These results, providing a detailed description of the proton damage effects in $PbWO_4$ crystals, represent fundamental information for the understanding of the future CMS ECAL performance in the high radiation environment of HL-LHC.

Acknowledgments

We would like to acknowledge our colleagues of the CERN SPS facility and all engineers and technicians whose work on the preparation of the test beam modules, their operation and data-taking, made these results possible. We also thank Maurice Glaser and Federico Ravotti who have been responsible for the proton irradiation at the CERN PS IRRAD facility. We are also grateful to the CMS Technical Coordination team who helped setting up the crystal exposure inside the CMS cavern.

References

[1] CMS collaboration, *The CMS experiment at the CERN LHC*, 2008 *JINST* **3** S08004.

[2] CMS collaboration, *The CMS electromagnetic calorimeter project: Technical Design Report*, CERN-LHCC-97-033 (1997) [CMS-TDR-4].

2016 JINST 11 P04012

[3] M.T. Lucchini et al., *Evolution of the response of the CMS ECAL and possible design options for calorimetry at the High Luminosity LHC*, *IEEE Nucl. Sci. Conf. Rec. (NSS/MIC)* (2013).

[4] I. Dafinei, E. Auffray, P. Lecoq and M. Schneegans, *Lead Tungstate for High Energy Calorimetry*, in *Symposium P — Scintillator and Phosphor Material. Volume 348*, P. Lecoq, W.M. Yen, R.C. Ruchti, M.J. Weber, C. Woody and R.-y. Zhu eds., Cambridge University Press (1994) [*MRS Proceedings* **348** (1994) 99].

[5] M. Nikl et al., *Luminescence and scintillation of single $PbWO_4$ crystals*, in proceedings of the *International Conference on Inorganic Scintillators and their Applications (SCINT95)*, Delft, The Netherlands, August 28–September 1 1995, pp. 257–259 [ISBN 90–407–1215–8].

[6] E. Auffray et al., *Scintillation characteristics and radiation hardness of PWO scintillators to be used at the CMS electromagnetic calorimeter at CERN*, in proceedings of the *International Conference on Inorganic Scintillators and their Applications (SCINT95)*, Delft, The Netherlands, August 28–September 1 1995, pp. 282–285 [ISBN 90–407–1215–8].

[7] CMS collaboration, *Radiation hardness qualification of $PbWO_4$ scintillation crystals for the CMS Electromagnetic Calorimeter*, 2010 *JINST* **5** P03010 [arXiv:0912.4300].

[8] E. Auffray et al., *Progress in the radiation hardness of PWO scintillators for the CMS calorimeter*, in proceedings of the *International Conference on Inorganic Scintillators and their Applications (SCINT97)*, Shanghai, P.R. China, September 22–25 1997, p. 199.

[9] R. Chipaux and O. Toson, *Resistance of lead tungstate and cerium fluoride to low rate γ irradiation or fast neutrons exposure*, in proceedings of the *International Conference on Inorganic Scintillators and their Applications*, Delft, The Netherlands, August 28–September 1 1995, DAPNIA-SED-95-03 (1995).

[10] A. Annenkov, M. Korzhik and P. Lecoq, *Lead tungstate scintillation material*, *Nucl. Instrum. Meth.* **A 490** (2002) 30.

[11] Crystal Clear collaboration, P. Lecoq, *Ten years of lead tungstate development*, *Nucl. Instrum. Meth.* **A 537** (2005) 15.

[12] M. Huhtinen, P. Lecomte, D. Luckey, F. Nessi-Tedaldi and F. Pauss, *High-energy proton induced damage in $PbWO_4$ calorimeter crystals*, *Nucl. Instrum. Meth.* **A 545** (2005) 63.

[13] P. Lecomte, D. Luckey, F. Nessi-Tedaldi and F. Pauss, *High-energy proton induced damage study of scintillation light output from $PbWO_4$ calorimeter crystals*, *Nucl. Instrum. Meth.* **A 564** (2006) 164.

[14] E. Auffray and A. Singovski, *Experimental Study of Lead Tungstate Scintillator Proton-Induced Damage and Recovery*, *IEEE Trans. Nucl. Sci.* **59** (2012) 2219.

[15] M. Anfreville et al., *Laser monitoring system for the CMS lead tungstate crystal calorimeter*, *Nucl. Instrum. Meth.* **A 594** (2008) 292.

[16] CMS collaboration, *The CASTOR calorimeter at the CMS experiment*, in proceedings of the *16th International Moscow School of Physics and 41st ITEP Winter School of Physics*, Moscow, Russia, February 12–19 2013 [arXiv:1304.2943].

[17] E. Auffray et al., *Performance of ACCOS, an Automatic Crystal quality Control System for the PWO crystals of the CMS calorimeter*, *Nucl. Instrum. Meth.* **A 456** (2001) 325.

[18] M. Glaser, F. Ravotti and M. Moll, *Dosimetry assessments in the irradiation facilities at the CERN-PS accelerator*, *IEEE Trans. Nucl. Sci.* **53** (2006) 2016.

2016 JINST 11 P04012

[19] RD2 collaboration, C. Furetta et al., *Fluence and dosimetric measurements for a $\pi^{\pm}$ irradiation facility*, *Nucl. Phys. Proc. Suppl.* **44** (1995) 503.

[20] M. Huhtinen, P. Lecomte, D. Luckey, F. Nessi-Tedaldi and F. Pauss, *High-energy proton induced damage in $PbWO_4$ calorimeter crystals*, *Nucl. Instrum. Meth.* **A 545** (2005) 63.

[21] G. Battistoni et al., *The FLUKA code: Description and benchmarking*, *AIP Conf. Proc.* **896** (2007) 31.

[22] A. Ferrari, P.R. Sala, A. Fassò and J. Ranft, *FLUKA: a multi-particle transport code*, CERN-2005-010 (2005) [SLAC-R-773] [INFN-TC-05-11].

[23] HAMAMATSU Photonics K.K. Electron tube division, *Photomultiplier tubes and assemblies for scintillating counters and high energy physics*, http://neutron.physics.ucsb.edu/docs/High_energy_PMT_TPMO0007E01.pdf.

[24] J. Spanggaard, *Delay Wire Chambers — A Users Guide*, SL-Note-98-023-BI (1998).

[25] *Charge Analog-to-Digital Converter*, http://teledynelecroy.com/lrs/dsheets/1182.htm.

[26] National Instruments Corp., *LabVIEW System Design Software*, http://www.ni.com/labview/.

[27] GEANT4 collaboration, S. Agostinelli et al., *GEANT4: A Simulation toolkit*, *Nucl. Instrum. Meth.* **A 506** (2003) 250.

[28] F. Gentit, *Litrani: A General purpose Monte Carlo program simulating light propagation in isotropic or anisotropic media*, *Nucl. Instrum. Meth.* **A 486** (2002) 35.

[29] M.J. Oreglia, *A study of the reactions $\psi' \to \gamma\gamma\psi$*, Ph.D. Thesis, Stanford University, Stanford U.S.A. (1980).

[30] CMS collaboration, *Energy Calibration and Resolution of the CMS Electromagnetic Calorimeter in pp Collisions at $\sqrt{s} = 7$ TeV*, 2013 *JINST* **8** P09009 [arXiv:1306.2016].

2016 JINST 11 P04012